Over-wing integration of ultra-high bypass ratio engines: A coupled wing redesign and engine position study

(article starts on next page)

Over-wing integration of ultra-high bypass ratio engines: A coupled wing redesign and engine position study

Vinícius Tavares Silva [a,*], Anders Lundbladh [b], Carlos Xisto [a], Tomas Grönstedt [a]

[a] Chalmers University of Technology, Hörsalsvägen 7A, SE-41296, Gothenburg, Sweden
[b] GKN Aerospace Sweden AB, Flygmotorvägen 1, SE-46138, Trollhättan, Sweden

ABSTRACT

The integration of next-generation high-bypass turbofan engines poses a major challenge to the aeronautical industry due to the larger fans necessary to achieve more fuel-efficient engines. The limited space underneath the wings and the strict ground clearance constraints bring the necessity to investigate solutions other than the conventional under-wing mounted engines. Over-wing installed nacelles have the potential to solve the ground clearance issue and, in addition, might reduce ground noise due to acoustic shielding from the wing. Nevertheless, a strong and complex coupling between aerodynamics and propulsion is the result of such integration choice, and traditional design practices may result in configurations with prohibitively high drag penalties. This paper presents a novel wing redesign method, specifically developed for over-wing mounted engines. The wing is reshaped to recover the spanwise lift distribution of the clean airframe (wing-body) configuration, for a single aisle airliner at a cruise condition. The wing redesign is conducted along with an engine position sensitivity study, in which the wing is reshaped for different engine axial and vertical positions. The coupling between propulsion and aerodynamics is thoroughly investigated, as well as the interaction and interference effects between the wing, pylon, and nacelle. Moreover, the best over-wing solution is compared to a baseline under-wing mounted nacelle. Results show that, by applying the developed method, an overall drag reduction of 17.65 counts, or 6.4%, was obtained, compared to the initial over-wing configuration, comprising the original wing and baseline engine position. Nonetheless, the best over-wing nacelle design is still 5.58 counts, or 2%, higher in overall drag compared to the baseline under-wing mounted nacelle case.

© 2023 The Author(s). Published by Elsevier Masson SAS. This is an open access article under the CC BY license (http://creativecommons.org/licenses/by/4.0/).

1. Introduction

Engines that power commercial transport aircraft have historically had their propulsive efficiency enhanced by moving toward lower fan pressure ratios (FPR) and higher bypass ratios (BPR). The latest advances in aero-engine technology, such as geared fans, allow for larger engines with higher BPRs to be developed. The next-generation turbofans will likely reach FPRs of 1.4 and below, and BPRs higher than 15, referred to as ultra-high bypass ratio (UHBPR) engines, and consequently will feature larger fans and nacelles than those of the state-of-the-art engines [1,2]. The vast majority of civil aircraft feature engines mounted under and upstream of the wings, and such configuration generally provides lower installation drag than other integration choices. Nonetheless,

as the engines get larger, their installation under the wings becomes harder, majorly due to strict ground clearance constraints that must be met for safe aircraft operation. Therefore, aircraft manufacturers might be forced to venture outside of the well-established under-wing nacelle (UWN) design practice. An over-wing nacelle (OWN) integration would eliminate the ground clearance problem, and allow for the installation of lighter and shorter landing gears. Moreover, in such a configuration, the ground noise can potentially be decreased due to the acoustic shielding provided by the wing. Other possible benefits of over-wing mounted engines are powered low-speed lift and reduced intake distortion at high-incidence/low-speed conditions [3].

Some disadvantages can be expected from OWN installations, such as a significant increase in noise perceived by the passengers, because the engines are closer to the cabin. For aft-mounted OWN installations, the center of gravity is moved rearward, requiring that the fuselage is moved forward relative to the wing. This shortens the tail moment arm and requires larger vertical and horizontal tails, and consequently more tail drag and weight. Another potential drawback is the fact that over-wing mounted engines are

Nomenclature

Roman letters

$\boldsymbol{e_d}$	Unity vector in the drag direction
$\boldsymbol{n}$	Unity normal vector
$\boldsymbol{V}$	Velocity vector
$\dot{m}$	Mass flow
A	Area
A_e	Effective area
c	Chord
C_d	Drag coefficient
C_l	Lift coefficient
C_p	Pressure coefficient
D	Drag
D_{fan}	Fan diameter
dS	Infinitesimal surface element for the computation of forces
F_G	Stream gauge forces
l, d, z	Aerodynamic frame of reference
L	Lift
L_I	Inlet length
M	Mach number
p	Static pressure
p_t	Total pressure
q	Dynamic pressure
R_{far}	Farfield radius
Re	Reynolds number
T	Static temperature
T_t	Total temperature
T_{net}	Standard net thrust
V	Velocity magnitude
x, r, ψ	Cylindrical coordinates
x, y, z	Cartesian coordinates

Greek letters

α_i	Local incidence angle
β	Local airfoil rotation
β_{te}	Airfoil trailing edge rotation
$\boldsymbol{\tau}$	Viscous stress tensor
ϵ	Camber angle
η	Spanwise location relative to the wing semi-span
ϕ	Wall and streamtube boundary forces
ϕ_{post}	Post-exit force
ϕ_{pre}	Pre-entry force
π_{rd}	Rotation-to-deformation ratio
ρ	Density
θ	Circumferential position on the nacelle and inlet

Subscripts and Superscripts

∞	Freestream
$*$	Modified
A	Airframe
bn	Bypass Nozzle
cc	Core cowl
cn	Core nozzle
hi	Highlight
$inst$	Installation
NAC	Nacelle
ref	Reference
$spin$	Spinner

Acronyms

AoA	Angle of attack
BC	Boundary condition
BPR	Bypass ratio
CRM	Common research model
FPR	Fan pressure ratio
OWN	Over-wing nacelle
RANS	Reynolds-averaged Navier Stokes
SST	Shear Stress Transport
UHBPR	Ultra-high bypass ratio
UWN	Under-wing nacelle
WB	Wing-body
WBPN	Wing-body-pylon-nacelle

harder to reach for maintenance, slowing operations and increasing costs.

It is well known that for OWN installations the noise is shielded by the wing and redirected above it. The potential for noise reduction of over-wing mounted engines has been studied since the 1970s, with promising results, such as in [4]. Recently, the effects of airframe acoustic shielding have been investigated for configurations such as the blended-wing-body, hybrid-wing-body, and more conventional tube-and-wing aircraft with over-wing mounted nacelles. Guo et al. have conducted noise prediction studies for a blended wing body configuration and concluded that, for aggressive assumptions on future technologies, such configuration can be 41.6 dB cumulative below the Federal Aviation Administration Stage 4 certification level [5]. Noise measurements were conducted by Doty et al. [6] for the hybrid-wing-body configuration, showing that airframe shielding combined with chevron nozzles achieved benefits of up to 10 dB. Moreover, Lorteau et al. [7] showed that a UWN configuration can be up to 12 dB noisier than an OWN configuration, at a position ahead of the airplane.

Despite the evident noise benefits, over-wing nacelle mounting acquired a bad reputation in the past since it would commonly be outperformed by UWN configurations, in terms of lift and drag. This is likely caused by high-pressure disturbances at the wing upper surface of the OWN configuration, leading to increased interference drag and lift penalties [8]. Nonetheless, a few OWN con-

figurations have been developed, such as the Fokker 614 and the HondaJet. Advanced optimization methods combined with modern computational fluid dynamics (CFD) might allow us to overcome the limitations from the past and design better conventional and advanced propulsion integration systems. Several methods have been developed for the design and optimization of aero-engine nacelles [9–14] and nozzles [15–17]. Additionally, extensive research has been conducted on UWN integration aerodynamics [18–22]. Therefore, new hopes have arisen for finding feasible OWN designs and renewed interest has been given to such configurations.

Some evidence exists that OWN integration can be an aerodynamically feasible solution, and that past evaluations may have failed to properly capture the interactions between wing, pylon, and nacelle shapes, along with the nacelle position. Fujino and Kawamura [23] have shown that the wave drag can be reduced, and the drag divergence Mach number increased, by placing an over-wing mounted nacelle at optimum axial and vertical positions relative to the wing, for an OWN business jet aircraft, without the need for reshaping the original laminar flow wing. Hill and Kandil [24] studied UWN and OWN configurations, and concluded that whilst the OWN integration led to higher overall drag at cruise, it provided a higher drag rise Mach number than that of the UWN configuration. Berguin and Mavris [25] pointed out the necessity of considering the interaction effects between the wing and nacelle shapes, along with the nacelle position, on the optimization
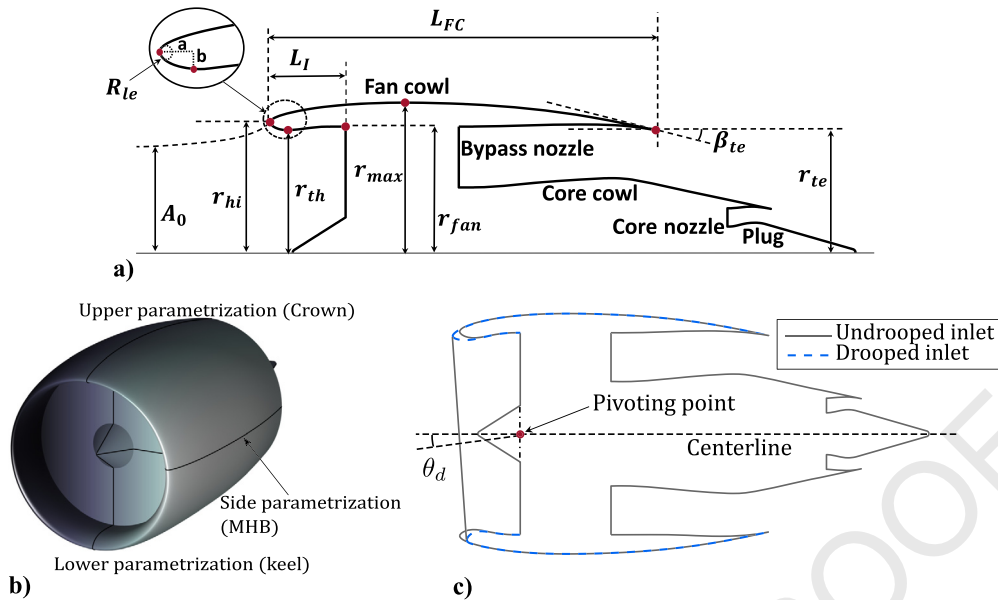
ARTICLE IN PRESS

JID:AESCTE   AID:108350 /FLA   [m5G; v1.335] P.3 (1-18)

V. Tavares Silva, A. Lundbladh, C. Xisto et al.   Aerospace Science and Technology ••• (••••) ••••••

Fig. 1. Nacelle geometry representation for: a) 2D nacelle profile, b) 3D geometry and c) drooped inlet [28].

of an OWN configuration, obtaining a drag reduction of 70% compared to an optimization process that merely varied the nacelle location. Hooker et al. [26] conducted several shape/nacelle position optimizations for different wing types, nacelle installations, and BPRs. They concluded that the most promising configuration was an OWN installation, featuring a low wing and trailing edge mounted engine and that OWN installations have a potential for increasing the aerodynamic efficiency (quantified as the freestream Mach number times the lift-to-drag ratio, $M_\infty L/D$) up to 5%, compared to the conventional UWN configuration. Furthermore, Lockheed is developing an innovative airlifter configuration, the Hybrid Wing Body, that comprises over-wing installed engines, and aims at a fuel saving of 70% compared to the C-17 airlifter [3,27].

Recently, Silva et al. [28] have compared UWN and OWN integrations of UHBPR engines. An increase in drag of 6.5% was obtained for the OWN configuration. Kaiyoom et al. [29] have carried out a coupled aeropropulsive design optimization of a wing and propulsor shape for an OWN configuration. Different engine sizes and placements were studied. Lange and Rudnik [30] have conducted axial and vertical engine position optimization studies for an OWN installation, achieving an 11% drag improvement compared to a baseline OWN location. Wegener [31], and Wegener and Lange [32], have investigated fuselage and wing-mounted OWN configurations, where wing twist and upper airfoil shape optimization were carried out. The optimized wing and fuselage mounted configurations provided about 20% and 9% additional drag, respectively, compared to a baseline UWN configuration. Furthermore, a sensitivity analysis of lift, drag and intake pressure recovery to variations in nacelle positions was carried out by Ahuja et al. [33] for an OWN configuration, followed by a wing shape optimization. Although the initial drag was reduced by 20%, the optimized OWN aircraft had 5% higher drag than that of their UWN baseline.

Over-wing nacelle integration has shown to be a complex problem, for which the coupling between airframe aerodynamics and propulsion is of major importance. This paper presents a novel methodology for conducting the aerodynamic integration design of an OWN configuration comprising a UHBPR engine and an ultra-short nacelle. The wing of the integrated configuration is reshaped to regain the spanwise lift distribution of the clean airframe (wing-body) configuration. The wing redesign is done in conjunction with an engine placement sensitivity study, meaning that, for each of

the evaluated nacelle positions, the wing is iteratively reshaped. A thorough investigation of OWN integration aerodynamics is carried out and special attention is given to the coupling between aerodynamics and propulsion. The wing, pylon, and nacelle interaction and interference effects are discussed in detail.

2. Methodology

An integrated design and aerodynamic evaluation framework was built in order to automatically carry out the calculations presented later in this work. The framework is comprised of geometry representation and integration with the airframe, automatic mesh generation, CFD computations, and thrust and drag bookkeeping. The framework elements as well as the utilized methods are described below.

2.1. Geometry representation

The nacelle and pylon geometries are generated by utilizing in-house tools [9] and subsequently integrated with an existing airframe shape [28]. The nacelle design and integration procedures are described as follows.

2.1.1. Nacelle

The Class Shape Transformation (CST) method [34,35] was used to generate the nacelle geometry used in this paper. The CST method has proven to be a versatile and robust approach for parametric geometry representation, being capable to create smooth aerodynamic shapes with few design variables. A CST shape is defined by a product between a class function, which defines the basic profile, and a shape function, which modifies the class function. The shape function is usually represented by a Bernstein polynomial [34,35]. In this work, a 2D nacelle geometry is comprised of six distinct CST curves, representing the inlet, fan-cowl, bypass nozzle, core-cowl, core nozzle, and plug. The main parameters necessary to represent a 2D nacelle geometry are shown in Fig. 1a. For a 3D nacelle design, shown in Fig. 1b, 2D profiles are generated at the positions $\psi = 0°$, $\psi = 90°$, and $\psi = 180°$ referred to as crown, maximum half-breadth (MHB) and keel, respectively, where ψ is the azimuth angle in a cylindrical coordinate system. The 3D shape is created by conducting sinusoidal interpolations in

V. Tavares Silva, A. Lundbladh, C. Xisto et al.   *Aerospace Science and Technology ••• (••••) ••••••*
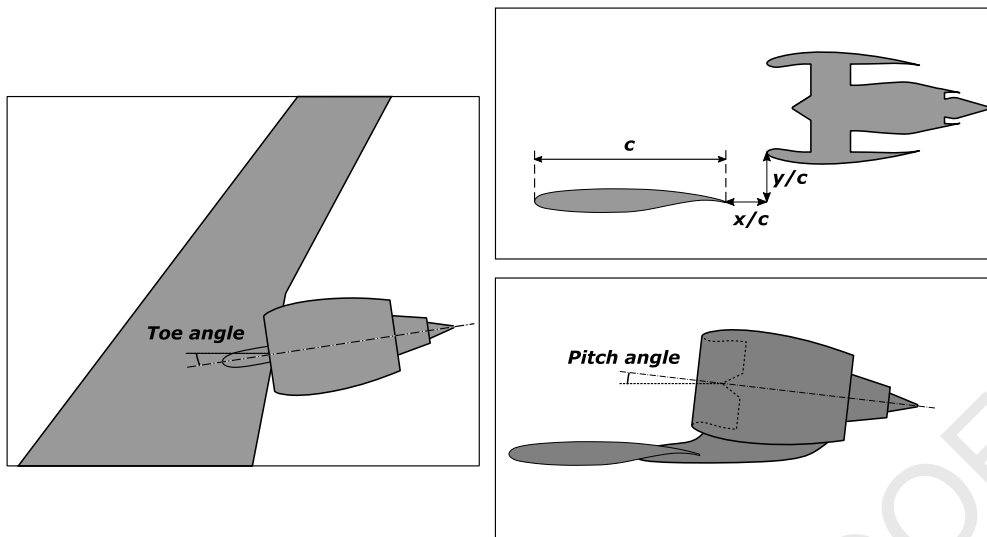

Fig. 2. Wing-body-pylon-nacelle geometry schematic representation. The toe and pitch angles are highlighted, along with the definitions for the relative axial and vertical locations.

r (radial coordinate) and x (axial coordinate) between the crown, MHB, and keel. The left nacelle half ($180° \leq \psi \leq 360°$) is a mirror image of the right half and the core engine is axisymmetric. Modern high-bypass turbofan nacelles are usually drooped for better alignment of the inlet with the incoming flow to reduce cruise drag. Fig. 1c shows an example of an asymmetric nacelle with a positively drooped inlet.

The test cases presented later in this work feature axisymmetric nacelles with ultra-short inlets, with an inlet length to fan diameter ratio (L_I/D_{fan}) of 0.3. The nacelles were designed by this paper's authors as part of the work conducted in [9], which presented a methodology for the multipoint design of ultrashort-nacelles, that considers the most critical operating conditions for the engine's performance and nacelle's design, such as cruise, high angle-of-attack (AoA), and crosswind. No installation effects were taken into account in the nacelle design process. The pylon geometries are generated by vertically stacking NACA 4-digit airfoils and are automatically adapted to changes in the engine location. The internal pylon bifurcations were not modeled for the current study.

2.1.2. Integration with the airframe

The nacelle and pylon were integrated with the NASA Common Research Model (CRM) wing-body (WB) aircraft geometry, which comprises a modern supercritical wing and a fuselage, representative of a wide-body commercial transport aircraft [36]. However, this work's object of study is narrow-body aircraft, and the nacelles were designed for an engine producing approximately the thrust level to power an A320. Therefore, the original CRM geometry was scaled down to the size of an A320, with respect to the reference chord (mean-aerodynamic chord), c_{ref}. The reference chord and area for the scaled aircraft are $c_{ref} = 4.194$ m, and $A_{ref} = 137.49$ m^2, respectively. The CRM's conventional tail was not included, since the over-wing integration usually requires a T-tail configuration.

For this study, the engine is installed downstream and above the wing's trailing edge. The main engine angles and positions are illustrated in Fig. 2. The wing's reference point is the trailing edge of the local airfoil, whereas the nacelle's reference point is the highlight of the keel profile. For the baseline OWN position, the normalized axial and vertical positions, x/c and y/c, were chosen to be 0 and 0.135, respectively, based on the optimum designs pre-

sented in [26]. Furthermore, the pitch and toe angles are equal to zero.

Moreover, in order to compare the final results, a baseline UWN configuration was selected. Its engine is installed at the same relative axial, vertical, and spanwise positions as the original CRM's nacelle, whose relative axial and vertical positions are $x/c = -0.706$, $y/c = -0.128$, respectively, with respect to the inlet's crown highlight, for pitch and toe angles equal to zero. For both the OWN and UWN configurations the nacelle was placed at a spanwise position η equal to 33% of the wing half-span. The positions x/c and y/c were assumed to be the most relevant ones, and thus were the object of the sensitivity study presented later in this work.

2.2. Numerical approach

Hybrid meshes were generated by means of the commercial meshing software POINTWISE. The surface meshes, generated with the quad-dominant algorithm, are comprised of quadrilaterals and triangles. For the near wall elements, the T-Rex algorithm was used to create anisotropic tetrahedra, hexahedra, prism, and pyramid elements, whereas the rest of the computational domain was populated with isotropic hexahedra layers with tetrahedra transitions, using the Voxel algorithm [37]. The computational domain is established between the semi-span aircraft geometry, a half-sphere (farfield), and a symmetry plane. The farfield radius, R_{far} was defined as a hundred times as large as the reference chord c_{ref}, as recommended in the fourth AIAA drag prediction workshop (DPW-IV) guidelines [38]. The height of the wall-adjacent cells was set so that $y^+ < 1$, in order to properly resolve the viscous sub-layer. Fig. 3 shows the surface and volume meshes used for the baseline OWN configuration, with the original CRM wing shape. A grid independence study is conducted later in this work (section 3.2). The baseline mesh for the selected refinement level was composed of approximately 81.6 million elements.

The CFD solver ANSYS FLUENT was used to resolve the Reynolds-Averaged Navier-Stokes equations (RANS) and compute the flow field for the cases presented in this paper. The pressure-based solver was utilized along with the pressure-velocity coupled algorithm. The turbulence closure was achieved by using Menter's $k - \omega$ shear stress transport (SST) turbulence model [39]. The least-squares cell-based method was used to calculate the flow field gradients, and the spatial discretization of the momentum and en-
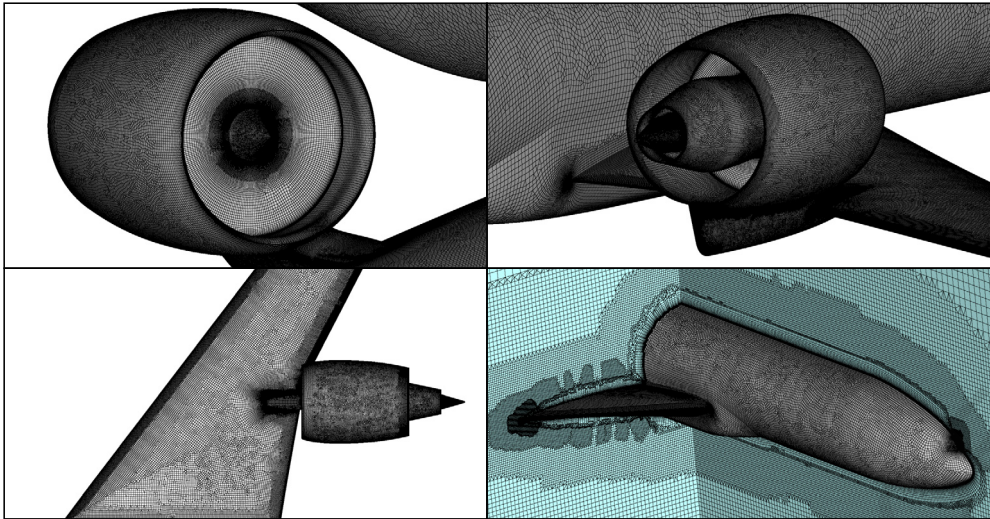
ARTICLE IN PRESS

JID:AESCTE   AID:108350 /FLA   [m5G; v1.335] P.5 (1-18)

V. Tavares Silva, A. Lundbladh, C. Xisto et al.   Aerospace Science and Technology ••• (••••) ••••••

Fig. 3. Surface and volume hybrid meshes for the OWN configuration. The meshes used in the computations carried out in is work are composed of approximately 82 million elements.
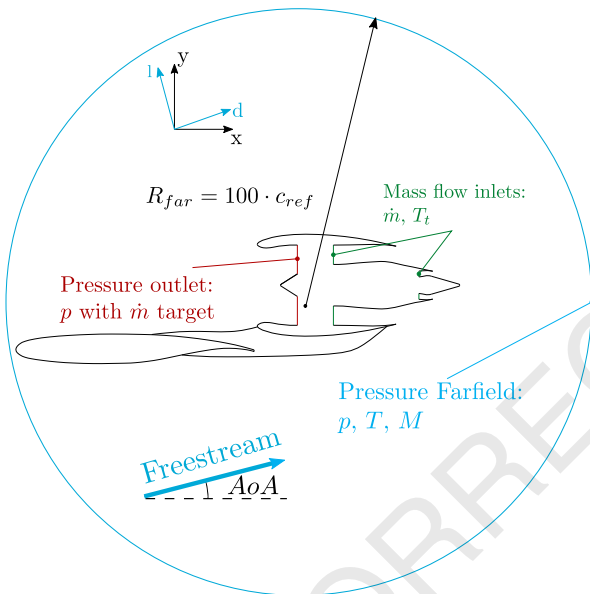

Fig. 4. Schematic representation of the computational domain and boundary conditions.

ergy equations was performed by using a second-order upwind scheme [40].

2.2.1. Boundary conditions

The schematic representation of the computational domain and boundary conditions (BC) for the CFD simulations is shown in Fig. 4. A pressure outlet BC is selected at the fan face, where the static pressure is iterated until a target mass flow is achieved. At the inlet of the core and bypass nozzles, a mass flow inlet BC was chosen, where mass flow and total temperature are specified. The external spherical domain is defined as a pressure far-field BC, where the Mach number, static pressure, static temperature, and flow direction are specified. All the airframe and nacelle surfaces are set to be no-slip adiabatic walls. The spinner, in particular, was modeled as a rotating wall, with a rotational speed of 3250 rpm. The commercial software GASTURB was used to calculate the engine's thermodynamic cycle and define the boundary conditions. The engine cycle chosen in this work is aimed to be representative of a notional UHBPR turbofan engine. The freestream boundary

conditions were selected for a typical narrow-body aircraft operating at cruise: a flight Mach number equal to 0.8 and an altitude of 35000 ft. The Reynolds number and reference temperature are respectively $Re = 26.4$ million and $T_\infty = 218.81$ K.

2.3. Thrust and drag bookkeeping

The formulation presented in [41] was used as the basis for the thrust and drag bookkeeping method presented in this work. Its derivation relies on integration over the nacelle and aircraft surfaces, and along the captured streamtube, therefore it is considered a modified near-field bookkeeping method. Fig. 5 shows a schematic representation of the forces acting on an OWN configuration powered by a two-stream turbofan. The undisturbed flow is not always parallel to the domains' axis, therefore, an aerodynamic frame of reference must be defined. In Fig. 5, x and y represent the aircraft reference frame, whilst l and d are the lift and drag axes, respectively, where d is parallel to the freestream and l perpendicular to it.

The forces acting on the nacelle, pylon, and aircraft wall surfaces, as well as on the captured and post-exit streamtubes' boundaries, can be expressed as follows:

$$\phi = \iint\limits_S [(p - p_\infty)\,\boldsymbol{n} + \boldsymbol{\tau} \cdot \boldsymbol{n}]\,dS \cdot \boldsymbol{e_d} \tag{1}$$

where $\boldsymbol{e_d}$ is the unit vector in the undisturbed flow direction. The stream gauge forces, F_G, can be defined as:

$$F_G = \iint\limits_S [\rho \boldsymbol{V}(\boldsymbol{V} \cdot \boldsymbol{n}) + (p - p_\infty)\boldsymbol{n}]\,dS \cdot \boldsymbol{e_d} \tag{2}$$

The infinitesimal surface element dS is computed at the lateral nacelle and captured streamtube surfaces for the calculation of ϕ, and at the passage areas for the computation of F_G.

The nacelle drag D_{nac} is defined as the integration of the viscous and pressure forces acting on the fan cowl ϕ_{cowl}, summed with the forces acting on the captured streamtube and exhaust plume, usually referred to as the pre-entry force ϕ_{pre}, and post-exit force, and ϕ_{post}, respectively [41], as follows:

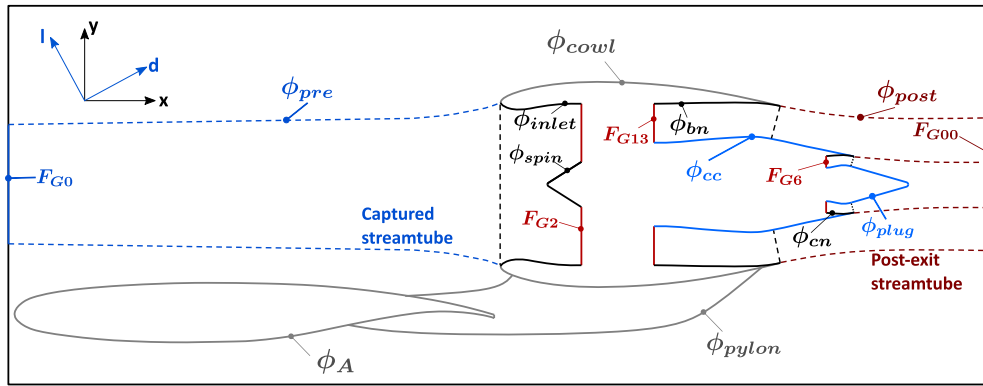$$D_{nac} = \phi_{pre} + \phi_{cowl} + \phi_{post} \tag{3}$$

Fig. 5. Forces acting on an over-wing mounted nacelle configuration, and definition of the aircraft and aerodynamic frames [28].

One of the challenges in computing nacelle drag from CFD calculations is the accurate prediction of ϕ_{post}. Because the downstream force F_{G00} is unknown, ϕ_{post} has to be computed by direct integration over the exhaust plume boundaries. Especially for integrated configurations, the post-exit streamtube will present complex flow patterns, deviating significantly from an axisymmetric shape expected for standalone nacelles. The integration approach requires the exact geometry of the post-exit streamtube, as well as a considerably high level of mesh refinement downstream of the nacelle, increasing significantly the computational cost of the simulations. For the aforementioned reasons, the computation of ϕ_{post} is often avoided. A common practice is to define the modified nacelle drag D^*_{nac}:

$$D^*_{nac} = \phi_{pre} + \phi_{cowl} \tag{4}$$

Although D^*_{nac} has been used plenty of times [20,21,42,43], it should be known that ϕ_{post} is normally a forward force (thrust direction) which can have a significant magnitude, as shown in [20], and thus, neglecting such term can lead to an over-prediction of the nacelle drag.

The nacelle net propulsive force F^{NAC}_{net} can be calculated by applying the conservation of momentum to an enclosed control surface around the nacelle, which results in the definition presented in Eq. (5):

$$F^{NAC}_{net} = F_{G13} + F_{G6} - F_{G2}$$
$$- (\phi_{bn} + \phi_{cc} + \phi_{cn} + \phi_{plug} + \phi_{cowl} + \phi_{spin} + \phi_{inlet}) \tag{5}$$

Different definitions for thrust are available in the literature [41–43]. The one employed in this study is referred to as modified standard net thrust T^*_{net}:

$$T^*_{net} = F_{G13} + F_{G6} - F_{G0} - (\phi_{bn} + \phi_{cc} + \phi_{cn} + \phi_{plug}) \tag{6}$$

where the term "modified" refers to the inclusion of the plug and core cowl external forces to the original form of the standard net thrust. The pre-entry drag is obtained by employing the conservation of momentum to the captured streamtube:

$$\phi_{pre} = F_{G2} - F_{G0} + \phi_{spin} + \phi_{inlet} \tag{7}$$

By substituting Eq. (6) and Eq. (7) into Eq. (5), F^{NAC}_{net} becomes:

$$F^{NAC}_{net} = T^*_{net} - \phi_{pre} - \phi_{cowl} = T^*_{net} - D^*_{nac} \tag{8}$$

The aircraft net propulsive force F_{net} and overall drag, of the wing-body-pylon-nacelle (WBPN) configuration, D_{WBPN} are defined by including the airframe and pylon drag, ϕ_A and ϕ_{pylon}, as follows:

$$F_{net} = T^*_{net} - \phi_{pre} - \phi_{cowl} - \phi_{pylon} - \phi_A$$
$$= T^*_{net} - D^*_{nac} - \phi_{pylon} - \phi_A \tag{9}$$

$$D_{WBPN} = D^*_{nac} + \phi_{pylon} + \phi_A \tag{10}$$

The installation drag D_{inst} is calculated by subtracting the wing-body drag D_{WB} from D_{WBPN}, for the same lift coefficient C_l, where D_{WB} is computed by integrating the pressure and viscous forces at the wing-body configuration's surfaces (Eq. (1)). The drag coefficient C_d can be defined by using the scaled CRM reference area A_{ref}, as follows:

$$C_d = \frac{D}{q_\infty A_{ref}} \tag{11}$$

where q_∞ is the dynamic pressure, $0.5\rho_\infty V_\infty^2$. Similarly, the lift coefficient is expressed as:

$$C_l = \frac{L}{q_\infty A_{ref}} \tag{12}$$

The drag forces are commonly expressed in terms of drag counts, where a count is the same as $10^4 C_d$. The mass flow ratio, MFR, is a reference aerodynamic performance parameter for inlets, and it is defined as the ratio between the streamtube captured area A_0 and the inlet highlight area A_{hi}, which is written as:

$$MFR = \frac{A_0}{A_{hi}} = \frac{\dot{m}_0}{\rho_0 V_0 A_{hi}} \tag{13}$$

It is worth noting that the exact definition of the inlet stagnation location is difficult for MFR $\neq 1$. Nevertheless, it is reasonable to assume that the flow will stagnate near the inlet highlight for a cruise condition. Therefore, the surfaces where ϕ_{cowl} and ϕ_{inlet} are computed were separated by the inlet highlight. In other words, ϕ_{inlet} is defined by integration on the inner inlet surface, whereas ϕ_{cowl} is computed at the external nacelle surface. Such simplification would lead to higher inaccuracy for low-speed and high-incidence conditions, where MFR is significantly higher than unity, resulting in flow stagnation at the external part of the inlet lip.

2.4. Wing reshaping procedure

In a study conducted by this paper's authors [28], it was observed that an over-wing mounted nacelle disturbs the upper wing flow field and causes a substantial lift reduction. It was shown that, although the lift can be easily recovered by increasing the aircraft AoA, the overall drag raises considerably, compared to a baseline UWN mount, due to a higher incidence, which leads to a stronger wing shock, and consequently higher wave drag. It was first attempted to mitigate the aforementioned drag increase by
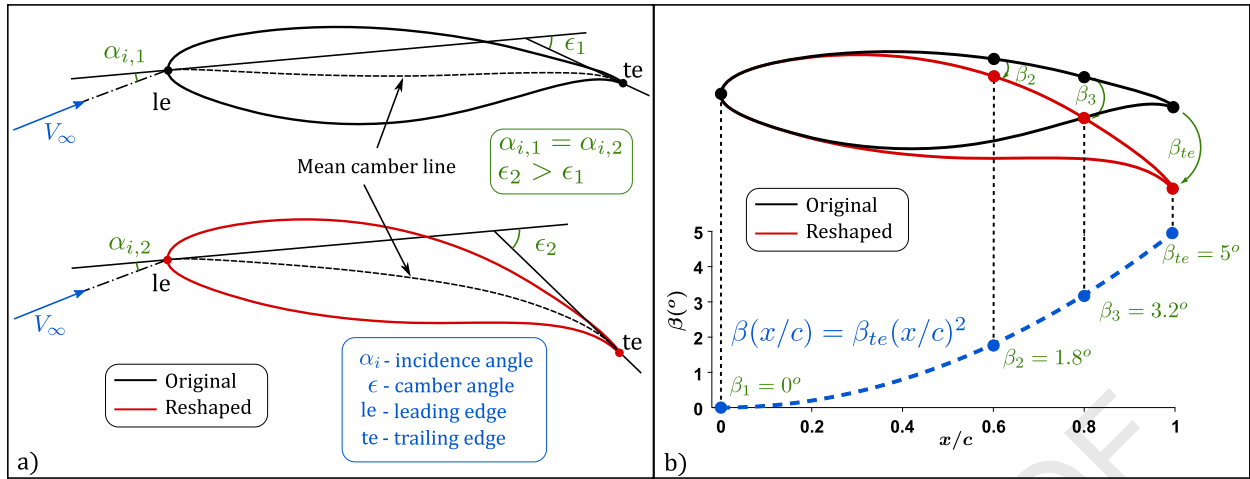
Fig. 6. Airfoil deformation process: a) definition of incidence and camber angles, b) airfoil deformed proportionally to a quadratic function for $\beta_{te} = 5°$.

re-twisting the wing locally, aiming to recover the sectional lift lost due to the engine integration. It was found that, although this method unloads the wing tip and thus decreases wave drag at the outboard portion of the wing, the incidence is substantially increased for the inboard wing, especially at the sections next to the pylon, which leads to a stronger shock and a net increase in wave and overall drag.

To overcome this problem, a novel method for reshaping the original wing is proposed. The method's goal is to recover the spanwise lift distribution of the wing-body configuration without a substantial increase in local incidence so that the net strength of the wing shock is not raised considerably. Due to the high computational cost of the CFD simulations, it was decided that the number of variables for the wing should be kept as low as possible. Therefore, the approach proposed here consists of jointly modifying the twist and camber at different wingspan locations by re-shaping the original airfoils. This is accomplished by locally deforming the airfoil for a given trailing edge rotation, β_{te}. The deformation is performed by employing local rotations to the airfoil's original shape, proportional to a quadratic function of the axial position. The local rotation angle $\beta(x/c)$ is calculated by the following expression:

$$\beta\left(\frac{x}{c}\right) = \beta_{te}\left(\frac{x}{c}\right)^2 \qquad (14)$$

where x/c is the axial position normalized by the airfoil's chord. Fig. 6a shows how the proposed method is able to maintain the airfoil's incidence, α_i, unchanged whilst increasing the camber angle, ϵ. Note that, because the trailing edge's position is being modified, the airfoil's twist will also not be the same. Fig. 6b illustrates how the airfoil deformation is accomplished for $\beta_{te} = 5°$. It can be seen that the farther from the leading edge the axial position is, the more pronounced becomes the local rotation.

It was initially thought that a combination of solid body rotation (twist) and airfoil deformation could lead to an optimum drag, therefore, the parameter rotation-to-deformation ratio, π_{rd}, was introduced. For $\pi_{rd} = 0$, the airfoil is purely rotated and for $\pi_{rd} = 1$, it is solely deformed. Fig. 7 shows how the airfoil geometry modification is conducted for a single airfoil. The original airfoil is compared with a purely deformed ($\pi_{rd} = 0$) and purely rotated ($\pi_{rd} = 1$) airfoil, as well as with a combination of deformation and rotation ($\pi_{rd} = 0.5$), for a total trailing edge rotation of 5°.

To investigate how the π_{rd} parameter impacts the airfoil's aerodynamic performance, 2D CFD simulations were carried out for
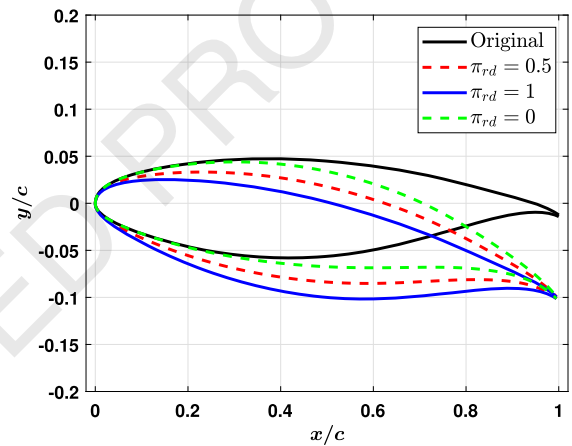

Fig. 7. Airfoil geometry reshape: pure deformation ($\pi_{rd} = 0$), pure rotation ($\pi_{rd} = 1$), or combined rotation/deformation ($\pi_{rd} = 0.5$) modifications.
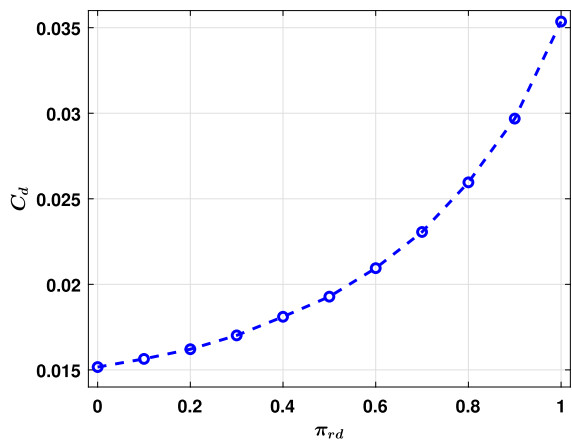

Fig. 8. Impact of the rotation-to-deformation ratio on the airfoil C_d.

a supercritical airfoil, whose original shape was modified according to the aforementioned method for a range of rotation-to-deformation ratios varying from zero (pure rotation) to unity. For each of the computations, the initial airfoil was reshaped to attain $C_l = 1.0$, for $M_\infty = 0.72$, $Re = 30 \times 10^6$, and a reference temperature of 300 K. The results depicted in Fig. 8 show that the airfoil C_d raises rapidly with the increase in π_{rd}, which is an indication that there is no benefit in applying a solid body rotation to the airfoil.

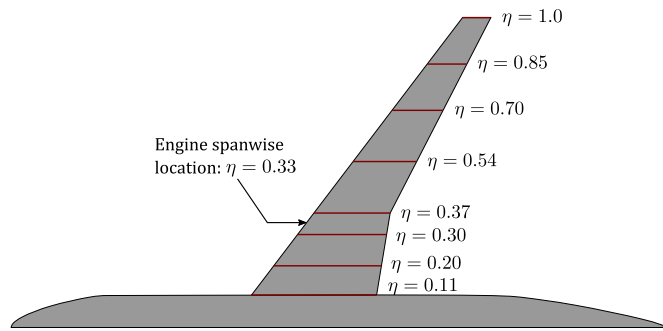V. Tavares Silva, A. Lundbladh, C. Xisto et al.

Fig. 9. Spanwise locations of the reshaped airfoils.

It is worth noting that this behavior can differ for the 3D wing, especially for installed configurations, for which the wing flow is disturbed by the engine. Nonetheless, it was assumed that similar behavior would be observed for the majority of the wing, and a pure deformation transformation ($\pi_{rd} = 0$) was employed for all the airfoils, except for that located at the wing tip ($\eta = 1.0$), which was purely rotated to maintain the original round wing tip shape. The modified 3D wing shape is generated by reshaping the airfoils at the 8 spanwise sections shown in Fig. 9. The original airfoils are simultaneously modified iteratively until the desired sectional lift distribution is achieved.

2.5. Aircraft equilibrium of forces

In order to compare the aerodynamic performance of different aircraft configurations, it is desirable that they are in an equilibrium of forces state. Therefore, not only C_l has to be the same, but also the aircraft's net propulsive force should be zero. Fig. 10 shows the flowchart of the adopted procedure to simultaneously obtain the target C_l and $F_{net} = 0$. Initially, the boundary conditions are defined based on the cycle data for an estimated required thrust. Next, a CFD simulation is performed for a guessed AoA and C_l is computed. The AoA is iterated until C_l reaches its target value. Subsequently, the mass flow at the fan face $\dot{m}_f$ is iterated until the condition $F_{net} = 0$ is satisfied, for the same BPR, and the boundary conditions are recalculated by means of isentropic flow equations for an ideal gas. For every change in $\dot{m}_f$, C_l is re-iterated. The target C_l used in this work was 0.5, the same as the CRM's. This method is used later in this paper (section 3.2.3) when comparing the OWN with the baseline UWN configuration.

As mentioned in section 2.1.2, the tails are not included in the configurations studied here. However, by neglecting the tail drag, the engine throttle condition for $F_{net} = 0$, would be underestimated. Therefore, the tail drag was estimated by using Raymer's drag component buildup method [44], for the computations carried out later in section 3.2.3.

3. Results and discussion

3.1. Numerical approach validation

The wing-body-pylon-nacelle NASA CRM geometry [36] was used to validate the numerical approach adopted in this work. A hybrid mesh with 49.16 million elements was generated by using the commercial software POINTWISE. The RANS CFD simulation was conducted by using the same numerical schemes, spatial discretization, and turbulence closure as described in section 2.2. According to the guidelines provided by the sixth AIAA drag prediction workshop (DPW-VI) [45], the computations were carried out for $M_\infty = 0.85$, $Re = 5 \times 10^6$, and $C_l = 0.5$. The simulations were compared against experimental results carried out at NASA's
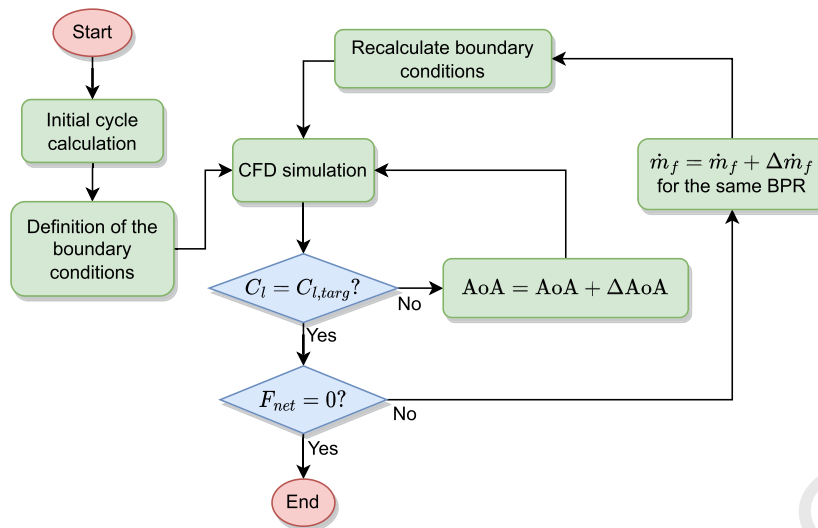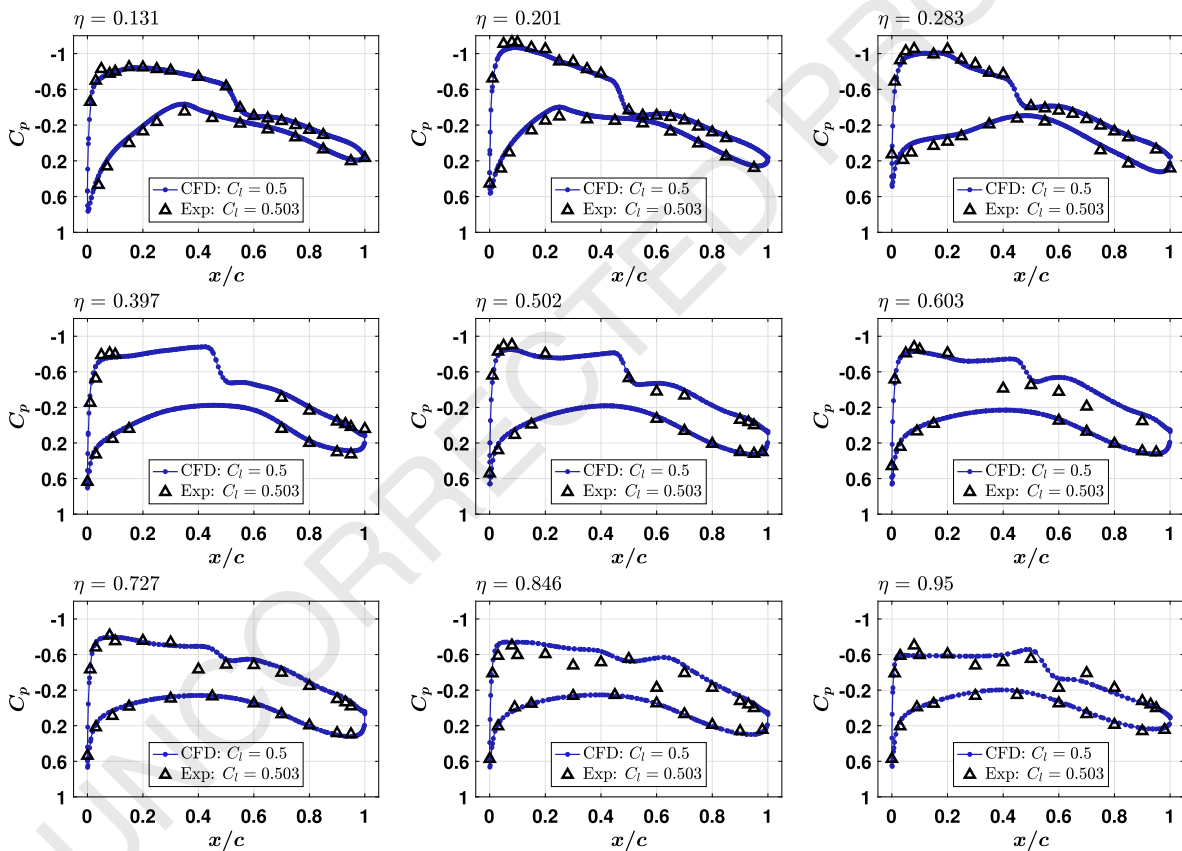
National Transonic Facility for the same Re, M_∞, and similar C_l, as depicted in Fig. 11. Although the results show a good overall agreement between the pressure coefficient, C_p, distributions for different wing span-wise locations, η, the differences increase as the span station approaches the wing tip. The same effect was observed in the DPW-VI [45], which can be attributed to the aeroelastic deformation of the CRM wing, which is the highest at its tip.

3.2. Mesh independence study

To ensure that the utilized grid was fine enough to compute the variables of interest, a mesh independence study was carried out. The study was conducted for six grids of increasing resolution, for an OWN configuration comprising the original CRM wing. The number of cells N ranged from 27.95×10^6 to 150.63×10^6 elements. A global scale factor was applied to the surface mesh in order to guarantee consistent mesh refinement. The height of the wall adjacent cells was kept constant for all the computations, nonetheless, the number of cells defining the boundary layer changes with the global scaling factor. The wall y^+ was less than unity for all the assessed grids. The selected boundary conditions are described in section 2.2.1. The mesh independence study results are depicted in Fig. 12a for C_d and in Fig. 12b for T^*_{net}, where a monotonic behavior can be observed. Due to the high computational cost of such computations, the grid with 81.62×10^6 cells was chosen for the cases presented later in this work. The percentage difference with respect to the finest grid is -0.82% (or -2.2 drag counts) for C_d and 0.1% for T^*_{net}. Moreover, it is worth noting that, for the chosen grid, the mesh generated around the nacelle presented similar refinement levels to previous work for standalone nacelles conducted by this paper's authors [9].

3.2.1. Reshaped wing

The wing reshaping procedure described in section 2.4, was applied to the original wing, for the baseline engine position. The aircraft AoA for which the wing-body configuration achieved $C_l = 0.5$ (AoA $= 2.35°$) was maintained during the reshaping process. The wing shape was iterated until all the selected locations attained a sectional lift within $\pm 0.5\%$ of the target value. Furthermore, for comparison with the reshaping method, a simpler total lift recovery method was applied to the original configuration, which consisted solely in adjusting the aircraft AoA for the same target C_l. The spanwise lift distributions for the two lift recovery methods are shown in Fig. 13. Fig. 13a depicts the spanwise lift distribution for the wing-body configuration, the OWN configuration having the original AoA, and the OWN configuration where the aircraft AoA was increased to achieve $C_l = 0.5$. It can be seen that the sectional lift decreases over the entire wingspan when the engine is installed. The lift-loss phenomenon has been widely described in literature [26,28,30–32], and can mainly be attributed to a pressure rise at the upper surface of the wing caused by diffusion in the captured streamtube, when MFR < 1. The lift can be easily recovered by increasing the AoA. As demonstrated in [28], this comes together with a drag penalty, caused by higher fuselage drag, higher wing wave drag, and unnecessary outboard wing loading (see 13a). Fig. 13b compares the spanwise lift distribution obtained with the new re-design method with that resulting from the increased AoA method. The amount of lift generated by the nacelle is not negligible, therefore the wing lift distribution, added to the nacelle lift distribution, was included in the plots of Fig. 13b. As mentioned in section 2.4, the airfoils are reshaped at the spanwise locations shown in Fig. 9, whereas the position where the sectional lift is targeted is shown in Fig. 13b. These positions are coincident, except for the wing root and tip, for which the location where the sectional lift is targeted is slightly moved outboard and

ARTICLE IN PRESS

JID:AESCTE   AID:108350 /FLA   [m5G; v1.335] P.9 (1-18)

V. Tavares Silva, A. Lundbladh, C. Xisto et al.   Aerospace Science and Technology ••• (••••) ••••••

Fig. 10. Flowchart of the procedure to obtain $F_{net} = 0$.

Fig. 11. Pressure distribution for different wing spanwise locations η, for the CFD and experimental data of the NASA CRM wing-body-pylon-nacelle configuration. $M_\infty = 0.85$, $Re = 5 \times 10^6$, and $C_l = 0.5$. For the experimental data, the test run with $C_l = 0.503$ was chosen.

inboard, respectively, so that the effects of the tip vortex and fuselage interference are reduced. For the spanwise sections located under the nacelle, $\eta = 0.3$ and $\eta = 0.37$, the nacelle sectional lift was added to the wing section lift during the iterative reshaping procedure. It can be seen from Fig. 13b, that the wing-body-pylon-nacelle configuration with the reshaped wing successfully recovers the sectional lift over the entire wingspan. Near the nacelle, a discontinuity can be observed in the lift distribution of the reshaped wing for the case including the nacelle lift (Fig. 13b, green plot), which is caused by the extra lift provided by the nacelle. However,

the somewhat inaccurate lift matching in that region had negligible influence on the overall lift.

Fig. 14 shows the spanwise twist distribution for the original wing-body configuration compared to that of the reshaped wing for the OWN configuration. The twist distribution for the reshaped wing is a result of the employed shape deformation method, that locally rotates the wing's trailing edge. Most of the wing reshaping is performed next to the spanwise engine location ($\eta = 0.33$), where the majority of the lift is lost. As mentioned in section 2.4, the wingtip airfoil, in particular, is purely rotated, which explains
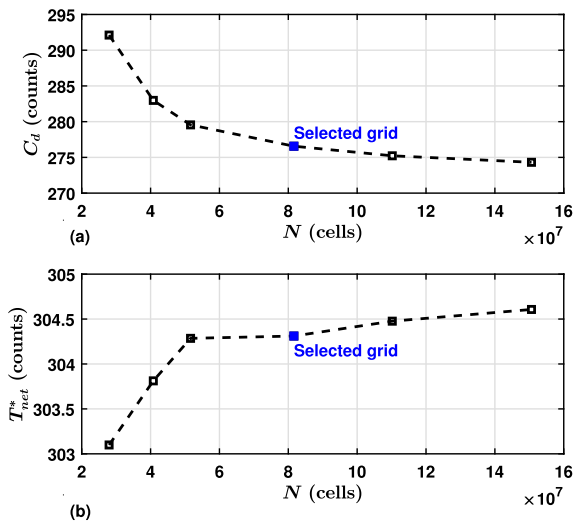
ARTICLE IN PRESS

JID:AESCTE   AID:108350 /FLA   [m5G; v1.335] P.10 (1-18)

V. Tavares Silva, A. Lundbladh, C. Xisto et al.   Aerospace Science and Technology ••• (••••) ••••••

Fig. 12. Mesh refinement results for a) C_d and b) T_{net}^*.

the increased twist near the tip region: since the camber remains unchanged, more twist is required to achieve the same amount of lift increment, compared to a purely deformed airfoil. Furthermore, it was found that reshaping a certain airfoil had an expressive impact on the lift of the neighbor airfoils, and this explains how the outboard portion of the wing, between $\eta = 0.7$ and $\eta = 0.9$, was able to recover the sectional lift without requiring to be highly reshaped.

The pressure contours and pressure distributions for the OWN configurations with the original and reshaped wings are depicted in Fig. 15, for $C_l = 0.5$. As a reference, the pressure distributions for the wing-body configuration were also included. The wing-body configuration AoA was equal to 2.35° for $C_l = 0.5$, which was maintained for the reshaped wing. For the original wing, the aircraft AoA was increased to 3.54°, for the same C_l. It can be noticed that, for the reshaped wing, the shock strength is significantly decreased over the entire wing semi-span. For wingspan positions next to the nacelle and pylon, such as $\eta = 0.3$ and $\eta = 0.37$, this phenomenon is more pronounced. Nonetheless, an undesirable flow behavior has been observed for the reshaped wing configuration: a local flow acceleration appears in the gap between the nacelle and the wing, especially outboard of the pylon, as can be observed in the $\eta = 0.37$ pressure distribution plot at Fig. 15. This leads the flow to choke and starts a secondary shock which propagates up to approximately 72% of the wing half-span. Such a phenomenon can be better understood by looking at Fig. 16, which presents the M contours at a longitudinal cut outboard of the pylon at the location $\eta = 0.37$ for a) the original wing and b) the reshaped wing. It is clear from Fig. 16b that, although the nacelle's relative position to the wing's trailing edge is the same, the reshaping method causes a larger boundary layer thickening towards the local airfoil's trailing edge, due to larger diffusion. This causes the effective area, A_e, between the nacelle and the wing to decrease and thus the flow accelerates more locally. As observed in [26], this acceleration, sometimes referred to as lip thrust, in moderate levels, might be beneficial to reduce nacelle pressure drag. Nevertheless, in the present case, it is responsible for creating a secondary shock on the wing's upper surface and, in more extreme cases, can lead the flow to separate across the nacelle/pylon intersection.

The main drag components of the OWN configuration are shown in Fig. 17 for the original and reshaped wings. The overall drag decreased by 8.1 counts, or 2.93%, after the wing was reshaped. Nonetheless, such a drag benefit was obtained not by lowering the wing drag, but due to a reduced nacelle and fuselage

drag. The fuselage drag reduction comes from the fact that the original AoA, from the wing-body configuration, was maintained, whilst the nacelle drag reduction is likely caused by the lip suction effect described above. On the other hand, the wing drag increased by 12.05 counts, or 8.3%, which is likely caused by an excessive wing reshaping, resulting from a non-optimal nacelle placement. Since the flow field around the wing is highly influenced by the engine's location, the final wing shape will also differ according to the engine's placement. Therefore, it is important to address the wing redesign and engine positioning as a coupled problem. The high increase in wing drag can be avoided by finding an optimum engine location that minimizes the amount of wing reshaping necessary to recover the target spanwise lift distribution. Therefore, an engine position sensitivity study will be carried out in the next section.

3.2.2. Engine position study

An engine position study, coupled with the reshaping strategy described in section 2.4, has been carried out, meaning that the wing was reshaped for every engine location. The main results are presented in Fig. 18. The relative axial and vertical positions, x/c and y/c, respectively, are defined with respect to the local chord's trailing edge. The engine spanwise location was maintained at a fixed $\eta = 0.33$. For some positions, boundary-layer separation occurred near the nacelle/pylon intersection. For such cases, the target sectional lift could not be obtained for the airfoils just inboard and outboard of the engine centerline ($\eta = 0.3$ and $\eta = 0.37$). Nonetheless, it was assured that the integrated C_l was equal to 0.5 for all cases. Each of the cases required between 9 and 15 computations to reach convergence of spanwise lift distribution. Fig. 18a shows the studied positions, where case A is the baseline nacelle position, case B is the best position and case C is an example of a bad location choice for which the flow is highly separated. It is worth noting that, during the reshaping process, only the relative positions are kept, meaning that the absolute engine position will vary according to the reshaped trailing edge's coordinates. In Fig. 18b, the overall aircraft C_d is depicted. The best engine location was: $x/c = 0.208$, and $y/c = 0.12$. It can be seen that both the axial and vertical positions have a major impact on the aircraft's drag, and it is generally a good idea to maintain the vertical position as low as possible, whereas it is advantageous to keep the engine downstream of the wing's trailing edge. Mounting the engines in vertical positions with y/c slightly lower than 0.12 could lead to lower overall drag, however, this would require a different pylon design, for which the pylon would have to reach the wing only from its lower surface, and thus such positions were not studied in this paper.

To better explain the overall drag results, Figs. 18c to 18f depict the drag of the main aircraft components. It was initially expected that the wing drag would reduce as the nacelle moves away from the wing. This is true for the axial position, however, as shown in Fig. 18c, a lower vertical position is beneficial for the wing drag. This can be explained by a negative wing interference drag as the engine approaches the wing vertically. Fig. 18d shows that the fuselage drag is mainly affected by the engine axial position. Fig. 18e depicts the nacelle C_d. It has been shown in section 2.4 that the nacelle and wing flow field strongly interact with each other, and, specifically for positions upstream of the wing trailing edge the flow accelerates quickly and chokes in the gap between the nacelle and wing. Although this phenomenon can cause several issues, such as an outboard wing shock or shock-induced separations on the nacelle and pylon, it can also contribute to a nacelle pressure drag reduction, due to a local forward force produced at the nacelle's lower lip. The low nacelle drag in Fig. 18e, when the engine is in close proximity to the wing, is a consequence of such a phenomenon. The pylon drag, shown in Fig. 18f, is influenced
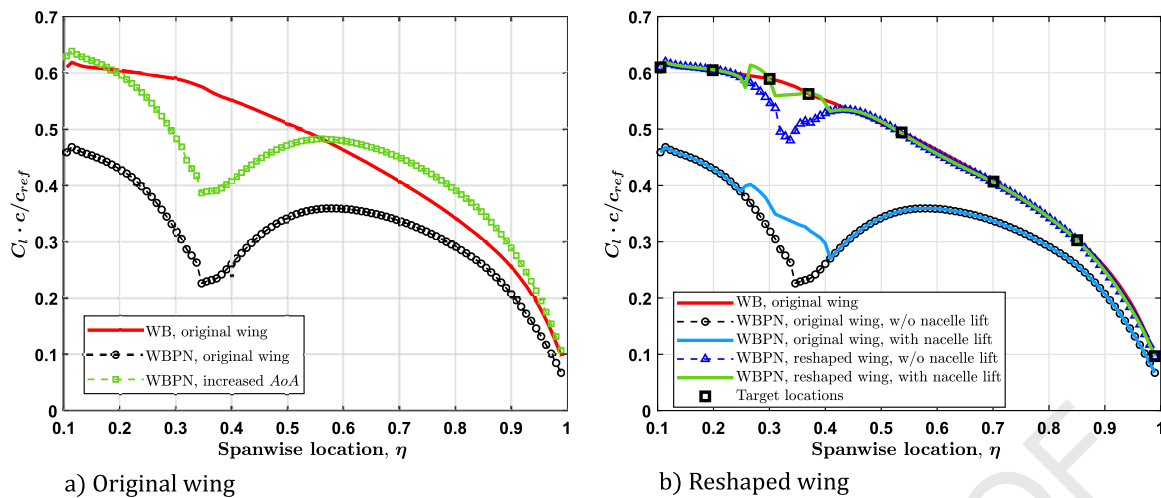
a) Original wing

b) Reshaped wing

Fig. 13. Spanwise lift distributions comparison for the two different lift recovery methods: a) original wing and b) reshaped wing (WB = wing-body and WBPN = wing-body-pylon-nacelle). The target locations refer to the spanwise positions where the sectional lift was targeted. (For interpretation of the colors in the figures, the reader is referred to the web version of this article.)
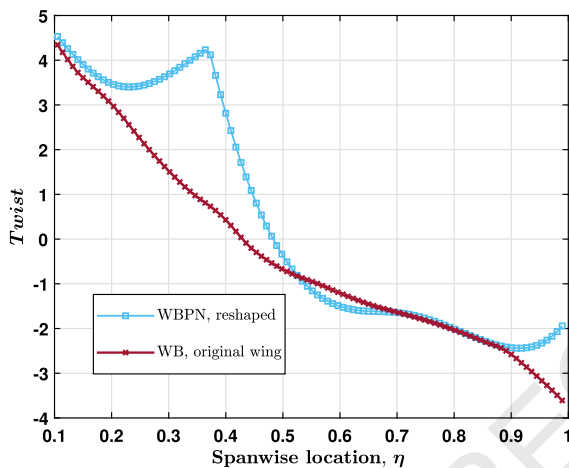

Fig. 14. Spanwise twist distributions for the original and reshaped wing. Note that the modified twist distribution for the reshaped wing is a direct consequence of the shape deformation method employed, which locally rotates the wing trailing edge.

by the pylon's wetted area, the interference with the nacelle and wing, and separations that are likely to occur at the pylon/nacelle intersection. The nacelle lip acceleration also contributes to pylon pressure drag reduction.

The contours of pressure distribution for cases A, B, and C are shown in Fig. 19a, Fig. 19b, and Fig. 19c, respectively. It can be observed that the high-pressure zone on the wing's upper surface, which is the major cause of the lift penalty, moves along with the engine axial position. Placing the engine downstream of the wings' trailing edge, as in case B, reduces both the area of high pressure and the magnitude of the pressure peak and, therefore, less deformation (twist and camber) has to be imposed to the wing so that it can recover the spanwise lift distribution. The main shock has similar strength for both three cases because the proposed reshaping method maintains the local wing incidence unchanged. Moreover, the strength of the secondary outboard shock formed at the wing will depend on the intensity with which the flow accelerates under the nacelle's lower lip. By placing the engine downstream of the wing's trailing edge, in case B, the gap acceleration effect was eliminated and the secondary wing shock vanished.

Fig. 20a, Fig. 20b, and Fig. 20c show the Mach number contours for cases A, B, and C, respectively, for the outboard spanwise section $\eta = 0.37$. It is seen that the more axially forward the na-

celle is relative to the wing, the more abruptly the flow accelerates around and below the lower nacelle lip, which can be explained by a local increase in mass flux. Case C is an example of how such lip acceleration can be detrimental to the aircraft aerodynamic performance: the acceleration zone reaches Mach numbers up to 1.49 and triggers a shock-induced separation on the nacelle and pylon. This increases the overall drag to prohibitive levels. On the other hand, the lip acceleration can be minimized by placing the engine downstream of the wing's trailing edge. Another interesting effect is the impact of the wing downwash on the captured streamtube. By comparing Fig. 20b, and 20c, it is easy to observe that, by placing the engine in a higher position, the amount of downward flow turning upstream of the nacelle's lower lip is reduced. This can have an impact on the amount of drooping necessary for the asymmetric nacelle design, not covered in this paper.

The aforementioned shock-induced separation on the nacelle and pylon is better illustrated in Fig. 21, for case C. It can be noticed that in the vicinity of the nacelle/pylon intersection, two large separation zones are formed in the outboard and inboard regions, which are induced by strong shocks. Although this is an extreme case, the separation-prone region at the pylon/nacelle intersection is still present for all the other cases studied, even if the flow is maintained fully attached. This could be problematic in the case of higher freestream Mach numbers.

The results previously presented in Fig. 17 are now compared with the drag results for the best nacelle position (see Fig. 22). The reshaped wing at the best position (case B) presented an overall C_d reduction of 9.55 drag counts, or 3.56%, with respect to the reshaped wing at the baseline position (case A), and of 17.65 drag counts, or 6.38%, with respect to the original wing, at the baseline position. The main advantage of optimizing the engine's position is to reduce the wing's drag because the pressure disturbances at the wing's upper surface are minimized and the final wing shape obtained for the target lift distribution is closer to the original geometry. Furthermore, it should be noted that the nacelle drag substantially raises in Case B. This occurs because, as the nacelle is moved downstream of the wing's trailing edge, the lower lip acceleration effect is weakened and eventually disappears, and so does its benefit to the nacelle pressure drag.

3.2.3. Over-wing and under-wing installations compared

In this section, the best OWN configuration (case B) is compared with a baseline UWN configuration. The same nacelle shape was used for both cases. The methodology described in section 2.5
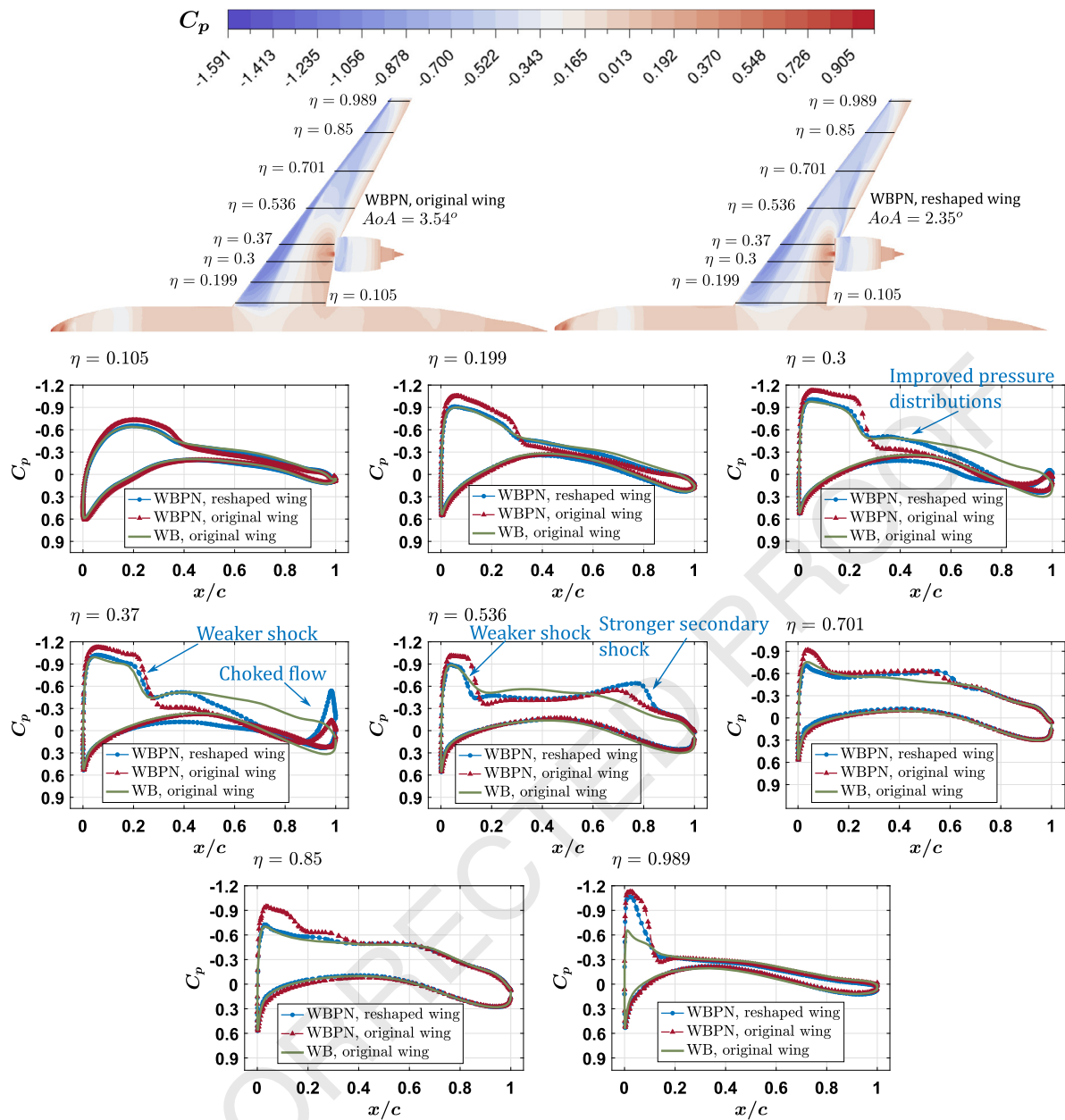
ARTICLE IN PRESS

JID:AESCTE   AID:108350 /FLA   [m5G; v1.335] P.12 (1-18)

V. Tavares Silva, A. Lundbladh, C. Xisto et al.   Aerospace Science and Technology ••• (••••) ••••••

Fig. 15. Pressure coefficient contours and pressure distributions for the WBPN (wing-body-pylon-nacelle) configuration with the original and reshaped wings, for $C_l = 0.5$. The pressure distributions of the wing-body (WB) configuration were included as a reference.

was utilized to obtain the $F_{net} = 0$ condition and assure that the forces in the freestream direction are in equilibrium, for $C_l = 0.5$. Moreover, to obtain a more realistic F_{net} prediction, the tail drag was estimated, as pointed out in the same section. To achieve $F_{net} = 0$ both the cases had to be throttled down from an initial MFR of 0.785 (for the initially specified fan boundary conditions) to MFR = 0.769 and MFR = 0.770, for the OWN and UWN configurations, respectively, for the same inlet highlight area. The pressure coefficient contours and wing pressure distributions for the OWN and UWN configurations are depicted in Fig. 23. At the inboard wing, the shock is the strongest for the latter, as can be observed in the pressure distributions for $\eta = 0.105$ to $\eta = 0.3$. On the contrary, the outboard wing shock is the strongest for the former, as shown in the pressure distributions for $\eta = 0.37$ and $\eta = 0.536$. For most of the outboard wing, the two mounting choices presented similar pressure distributions, with the exception of the wing tip, where, for the OWN, a higher leading edge acceleration

was necessary to recover the sectional lift of the wing-body configuration. Although not thoroughly investigated in this work, the engine spanwise position seems to impact both the wing shock strength and position. It can be seen in both cases that the shock is the strongest next to the pylon's spanwise location. For the OWN configuration, the shock is the strongest ahead of the high-pressure zone at the wing's upper surface (see the pressure contours in Fig. 23), as a way of partially balancing the lift lost in that region. For the UWN configuration, the shock strength and position seem to be determined by the pylon location, since the shock quickly vanishes on the outboard wing.

Fig. 24 depicts the C_p contours and pressure distributions on the nacelle and pylon, for the UWN and OWN configurations, where θ represents the circumferential location, starting at the nacelle's keel and increasing counter-clockwise. For the UWN configuration, the inboard and outboard flow behavior differ substantially. Whilst the outboard pressure contours are somewhat similar
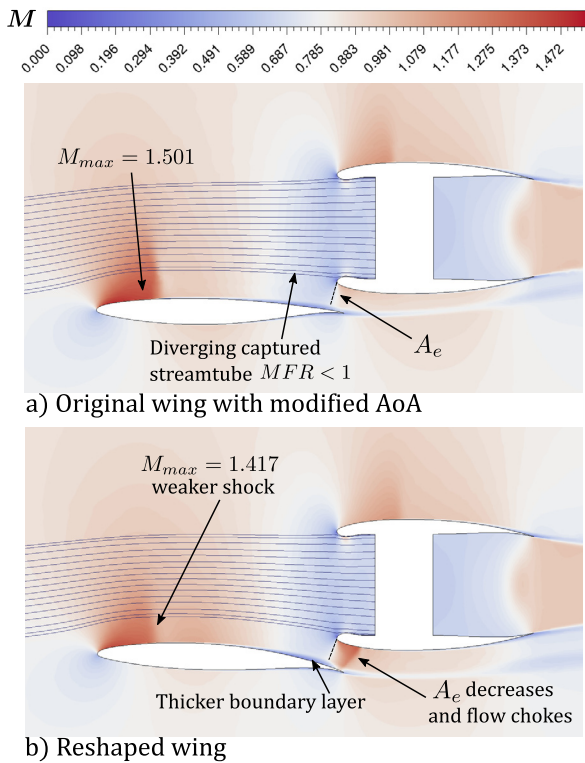
V. Tavares Silva, A. Lundbladh, C. Xisto et al.   *Aerospace Science and Technology ••• (••••) ••••••*

Fig. 16. Contours of Mach number for a) the original wing and b) reshaped wing, for $C_l = 0.5$, at the spanwise station $\eta = 0.37$.
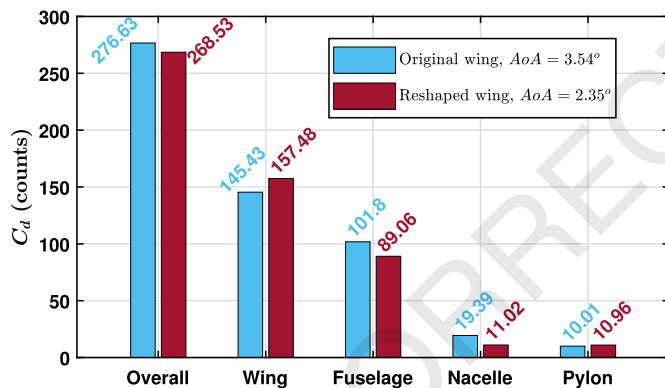

Fig. 17. Drag comparison between the original and reshaped wings, for $C_l = 0.5$.

to what would be expected from an uninstalled nacelle, the inboard flow is strongly affected by aerodynamic interference with the wing and pylon. It can be noticed that the flow stagnates at the pylon's inboard surface, which has an upstream effect on the inboard nacelle, causing the pressure to rise on the latter's upper half. On the other hand, a low-pressure zone can be observed on the lower half of the inboard nacelle, at its aftbody. This effect can be seen as a redistribution of momentum since the flow has to accelerate in the channel formed between the fuselage, wing, pylon, and inboard nacelle. Moreover, the UWN configuration shock covers only the upper part of the nacelle, sweeping an area between stations $\theta = 135°$ and $\theta = 270°$. The inboard shock is weaker compared to the outboard one, which is due to an outward flow deflection caused by the aircraft nose, and wing crossflow, resulting in a positive yaw incidence, and raising the inboard pressure at the lip. The overall drag could be further improved by aligning the engine better with the incoming flow, i.e., positioning the nacelle at an optimum toe angle.

For the OWN configuration, the wing downwash reduces the inlet incidence, increasing the pressure at the upper part of the cowl, compared to its lower part, and thus weakens the shock locally. A mild shock sweeps circumferentially the vast majority of the cowl annulus, however, the shock strength is suddenly increased in the vicinity of the pylon/nacelle intersection, as can be seen in the pressure distributions shown for station $\theta = 15°$, $\theta = 45°$, $\theta = 315°$, and $\theta = 345°$. This may be attributed to the overlapping effects of the flow acceleration around the nacelle lip and pylon nose. For the OWN configuration, the engine is located behind the wing, therefore the flow deflected by the aircraft nose had time to be straightened by the fuselage and thus the yaw incidence is not as prominent as for the UWN configuration. This is an indication that toe-angles might be of marginal importance for over-wing installed nacelles.

The drag results for the OWN and UWN configurations are shown in Fig. 25, now including the estimated tail drag. The drag of the OWN configuration is 5.58 counts, or 2%, higher than that of the UWN configuration. The reshaped wing has 8.23 counts, or 6.65%, more drag than the original wing for the UWN configuration. The fuselage drag is 1.53 counts, or 1.71%, lower for the OWN configuration. The nacelle drag is 31.66% lower and the pylon drag is 10.73 times higher for the OWN configuration, compared to the UWN mount. Although the nacelle and pylon drag differs substantially between the two installation choices, due to the previously mentioned pylon/nacelle interference effects, their sum differs solely in 1.13 counts. Furthermore, the obtained lift-to-drag ratio was equal to 17.95 and 17.59 for the UWN and OWN configurations, respectively.

A significant amount of effort has been put into the design of the wing-body-pylon-nacelle CRM geometry [36]. However, it is worth reminding the reader that the UWN configuration case presented in this paper has a different nacelle than the original CRM design (placed at the same axial and vertical locations). Moreover, the nacelles studied here are powered, which results in an additional interference between the exhaust system and the wing, causing an extra drag contribution referred to as blowing drag [46]. The CRM has flow-through nacelles, and the blowing drag effect has not been taken into account in the CRM's nacelle position optimization [36]. The UWN case presented in this paper could have achieved an improved performance in case the engine position was selected considering powered nacelles and the blowing drag effect. Nonetheless, it was assumed that the original CRM nacelle location would be a reasonable case for comparison with the OWN configuration designed in this work.

As much improvement is still required on the design methods for OWN installation, the results indicate that over-wing mounted engines might be a feasible solution in a near future. The method proposed for the wing redesign is relatively simple (only one variable per spanwise section), no modifications were done to the nacelle design, and to the spanwise engine position. Moreover, the nacelle toe and pitch angles were not investigated. The authors believe that, with more complete and integrated wing, nacelle, and engine position optimizations, OWN configurations with aerodynamic performance comparable to or better than the state-of-the-art aircraft can be designed.

4. Conclusion

This paper presented an aeropropulsive performance evaluation of an OWN configuration. A new wing redesign method, to be specifically applied for over-wing mounted engines, was presented. The method was coupled with an engine position sensitivity study, where 23 engine locations were analyzed. For each one of them, the original wing was reshaped to recover the spanwise lift distribution of the wing-body configuration. The coupling between
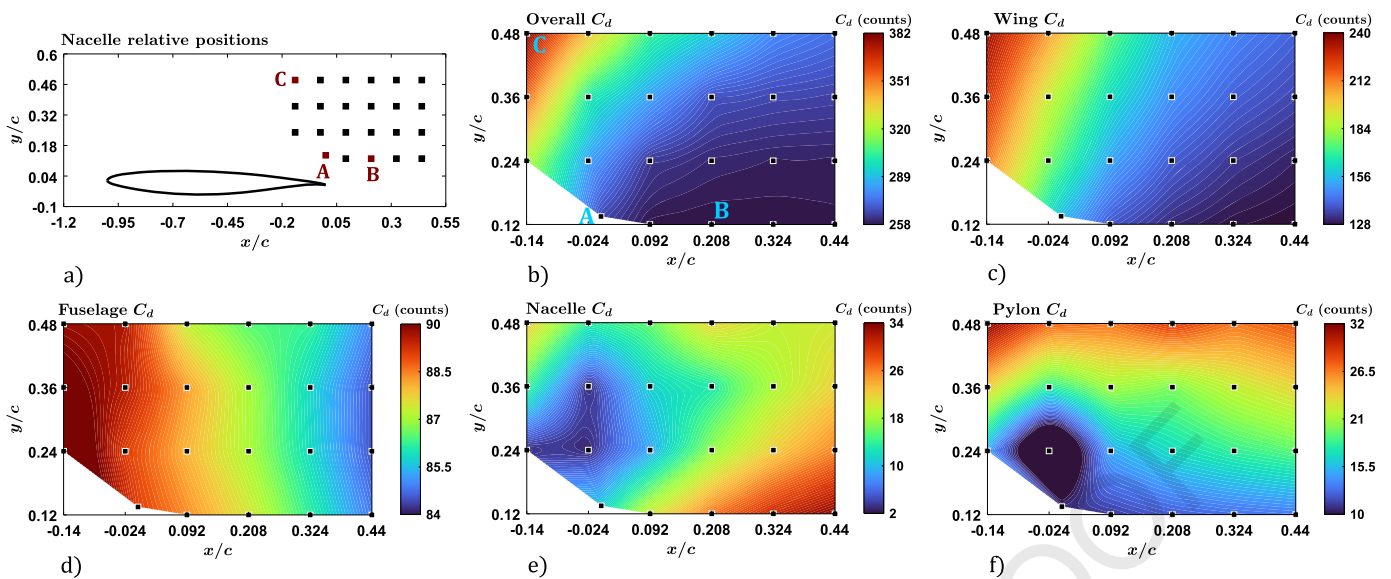
ARTICLE IN PRESS

JID:AESCTE   AID:108350 /FLA   [m5G; v1.335] P.14 (1-18)

V. Tavares Silva, A. Lundbladh, C. Xisto et al.   Aerospace Science and Technology ••• (••••) ••••••

Fig. 18. Nacelle position sensitivity study. The wing is reshaped to obtain the target spanwise lift distribution. The axial and radial positions are normalized by the local chord. The spanwise location is kept fixed at $\eta = 0.33$. $C_l = 0.5$ for all cases.
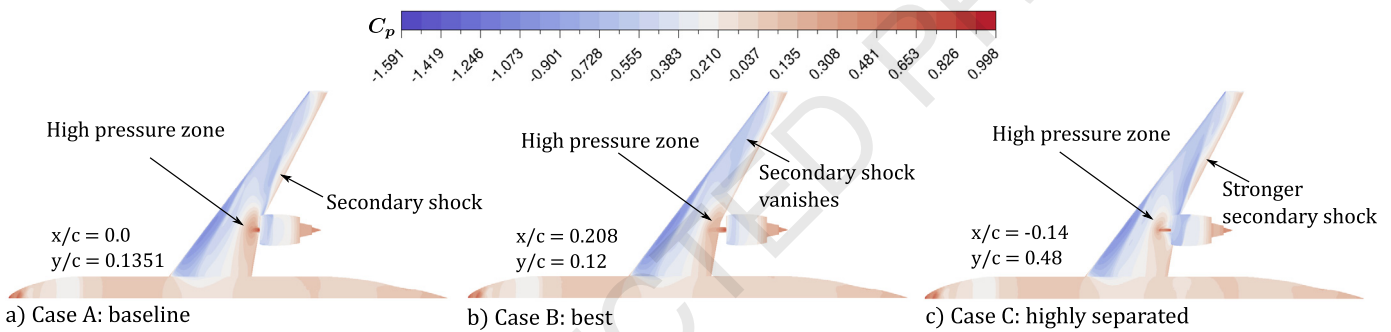
Fig. 19. Contours of pressure coefficient for: a) case A (baseline), b) case B (best position), and c) case C (highly separated). $C_l = 0.5$ for all cases.
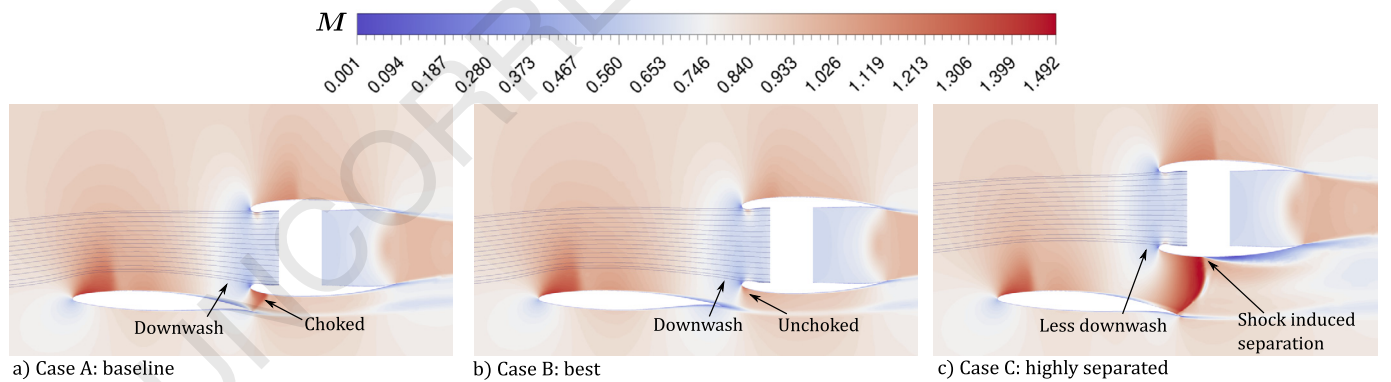

Fig. 20. Mach number contours at the spanwise station $\eta = 0.37$ (outboard of the nacelle) for a) Case A (baseline), b) Case B (best position), and c) Case C (highly separated). $C_l = 0.5$ for all cases.

aerodynamics and propulsion was thoroughly investigated for the OWN configuration. The best OWN design was compared to a baseline UWN configuration. The main findings obtained in this study are underlined next:

- The coupling between propulsion and aerodynamics is considerably stronger for over-wing installed nacelles than it is for conventional under-wing mountings. Positioning the engines over and downstream of the wings disturbs the flow and causes a sectional lift reduction throughout the entire

wingspan. Diffusion in the captured streamtube results in a high-pressure zone ahead of the nacelle, which is the major contributor to the overall lift loss. Not considering the integration effects on the wing design will likely result in a stronger wing shock, and excessive wave drag. For such reasons, a good OWN design requires the disciplines of aerodynamics and propulsion to be treated in conjunction. The classical approach, for which the wing and nacelle are designed separately and put together in a later design stage is no longer a feasible practice.
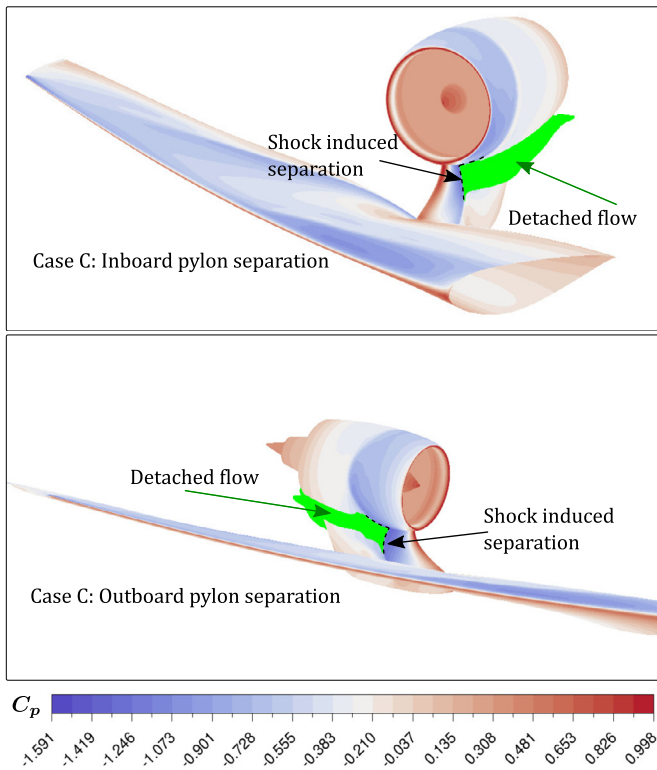
ARTICLE IN PRESS

JID:AESCTE AID:108350 /FLA   [m5G; v1.335] P.15 (1-18)

V. Tavares Silva, A. Lundbladh, C. Xisto et al.   Aerospace Science and Technology ••• (••••) ••••••

Fig. 21. Inboard and outboard shock-induced separation, starting at the nacelle/pylon junction in Case C. The separation zone is delimited by an iso-surface of zero axial velocity.
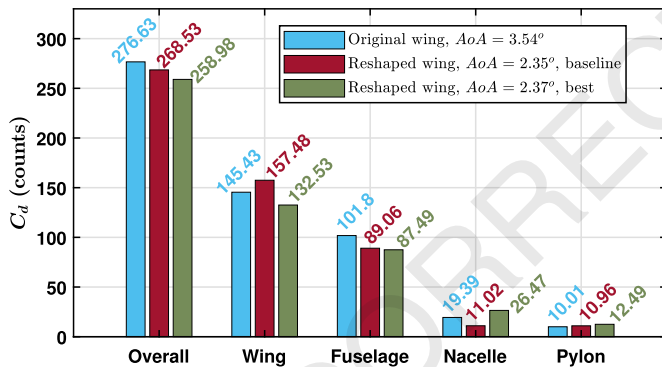

Fig. 22. Drag results for the following configurations: original wing, baseline reshaped wing (case A), and best position reshaped wing (case B). $C_l = 0.5$ for all cases.

- The developed reshaping method was successful in recovering the spanwise lift distribution of the wing-body configuration. Moreover, reshaping the wing resulted in an overall wing shock strength reduction. Nonetheless, the wing drag can increase considerably if the engine position is not properly selected. The main reasons for that are excessive boundary layer growth toward the trailing edge for highly reshaped airfoils, and excessive acceleration in the channel between the nacelle and the wing's upper surface. The latter may trigger a secondary wing shock formation.
- For the OWN configuration, a separation-prone region is formed in the vicinity of the nacelle/pylon intersection, caused by the overlapping between the nacelle and pylon shocks. For inadequate engine locations, especially upstream of the wing's trailing edge, large shock-induced separations can occur, resulting in a prohibitive rise in overall drag. Due to the complex

interactions between nacelle, pylon, and wing, it is highly recommended that the engine position studies are carried out including a pylon geometry.
- By employing the developed method, an overall drag reduction of 6.4% was achieved compared to the initial OWN configuration. The best OWN design is still 2% higher in drag compared to the baseline UWN mount. These results indicate that, in a near future, OWN configurations could consist of a feasible integration option, given that the existing design methods are still not fully matured.

This study only considered the high-speed aerodynamic aspects of OWN integration. Other benefits such as lighter landing gears, reduced ground noise, low-speed powered lift, and lower inlet distortion are potential benefits that can increase the likelihood for such an installation choice to become feasible in a near future.

Declaration of competing interest

The authors declare that they have no known competing financial interests or personal relationships that could have appeared to influence the work reported in this paper.

Data availability

Data will be made available on request.

Acknowledgements

References

[1] A. Magrini, E. Benini, H.-D. Yao, J. Postma, C. Sheaf, A review of installation effects of ultra-high bypass ratio engines, Prog. Aerosp. Sci. 119 (2020) 100680, https://doi.org/10.1016/j.paerosci.2020.100680.

[2] C. Hughes, D.V. Zante, J. Heidmann, Aircraft engine technology for green aviation to reduce fuel burn, in: 3rd AIAA Atmospheric Space Environments Conference, 2011, p. 3531.

[3] A.T. Wick, J.R. Hooker, C.M. Clark, R. Plumley, C. Zeune, Powered low speed testing of the hybrid wing body, in: 55th AIAA Aerospace Sciences Meeting, 2017, p. 0100.

[4] M. Reshotko, J.H. Goodykoontz, R.G. Dorsch, Engine-over-the-wing noise research, J. Aircr. 11 (4) (1974) 195–196.

[5] Y. Guo, C.L. Burley, R.H. Thomas, On noise assessment for blended wing body aircraft, in: 52nd Aerospace Sciences Meeting, 2014, p. 0365.

[6] M.J. Doty, T.F. Brooks, C.L. Burley, C.J. Bahr, D.S. Pope, Jet noise shielding provided by a hybrid wing body aircraft, in: 20th AIAA/CEAS Aeroacoustics Conference, 2014, p. 2625.

[7] M. Lorteau, L. Wiart, V. Kopiev, S.L. Denisov, Numerical study, with experimental validation, of fan noise installation effects in over-wing nacelle configuration using the immersed boundary method, in: 25th AIAA/CEAS Aeroacoustics Conference, 2019, p. 2519.

[8] D. Kinney, A. Hahn, P. Gelhausen, D. Kinney, A. Hahn, P. Gelhausen, Comparison of low and high nacelle subsonic transport configurations, in: 15th Applied Aerodynamics Conference, 1997, p. 2318.

[9] V.T. Silva, A. Lundbladh, O. Petit, C. Xisto, Multipoint aerodynamic design of ultrashort nacelles for ultrahigh-bypass-ratio engines, J. Propuls. Power 38 (4) (2022) 541–558, https://doi.org/10.2514/1.B38497.

[10] F. Tejero, M. Robinson, D.G. MacManus, C. Sheaf, Multi-objective optimisation of short nacelles for high bypass ratio engines, Aerosp. Sci. Technol. 91 (2019) 410–421, https://doi.org/10.1016/j.ast.2019.02.014.
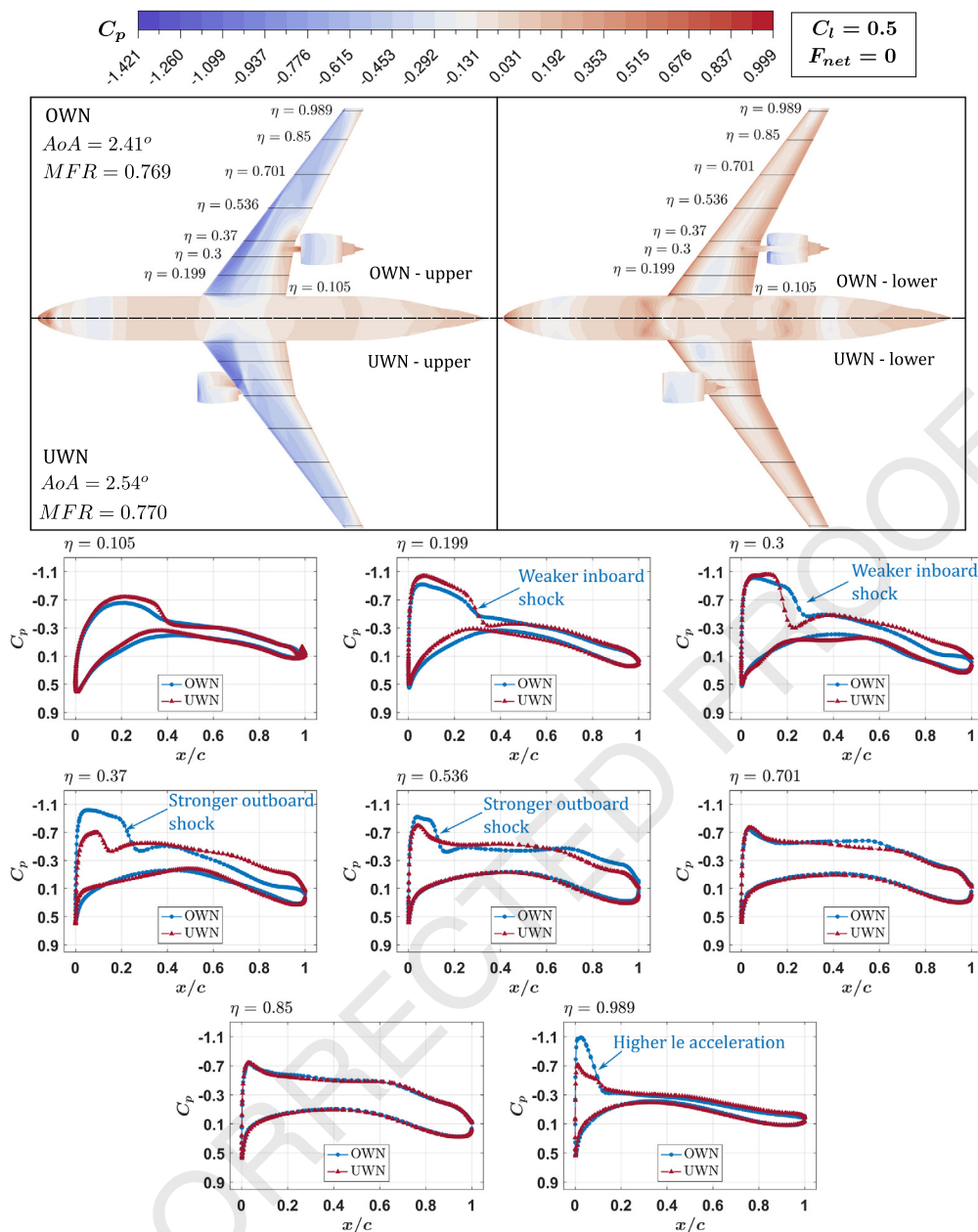
Fig. 23. Contours of pressure coefficient and wing pressure distributions for the baseline UWN and the best OWN configurations. $C_l = 0.5$ and $F_{net} = 0$.

[11] F. Tejero, D.G. MacManus, C. Sheaf, Surrogate-based aerodynamic optimisation of compact nacelle aero-engines, Aerosp. Sci. Technol. 93 (2019) 105207, https://doi.org/10.1016/j.ast.2019.05.059.

[12] F. Tejero, R. Christie, D. MacManus, C. Sheaf, Non-axisymmetric aero-engine nacelle design by surrogate-based methods, Aerosp. Sci. Technol. 117 (2021) 106890, https://doi.org/10.1016/j.ast.2021.106890.

[13] A. Peters, Z.S. Spakovszky, W.K. Lord, B. Rose, Ultrashort nacelles for low fan pressure ratio propulsors, J. Turbomach. 137 (2) (2014), https://doi.org/10.1115/1.4028235.

[14] V.T. Silva, A. Venkatesh, M. Lejon, A. Lundbladh, C. Xisto, Multipoint aerodynamic design of a nacelle for an electric fan, in: 33rd ICAS Congress, 2022.

[15] I. Goulos, T. Stankowski, J. Otter, D. MacManus, N. Grech, C. Sheaf, Aerodynamic design of separate-jet exhausts for future civil aero-engines—part I: parametric geometry definition and computational fluid dynamics approach, J. Eng. Gas Turbines Power 138 (8) (2016), https://doi.org/10.1115/1.4032649.

[16] I. Goulos, J. Otter, T. Stankowski, D. MacManus, N. Grech, C. Sheaf, Aerodynamic design of separate-jet exhausts for future civil aero-engines—part II: design space exploration, surrogate modeling, and optimization, J. Eng. Gas Turbines Power 138 (8) (2016), https://doi.org/10.1115/1.4032652.

[17] J.J. Otter, R. Christie, I. Goulos, D.G. MacManus, N. Grech, Parametric design of non-axisymmetric separate-jet aero-engine exhaust systems, Aerosp. Sci. Technol. 93 (2019) 105186, https://doi.org/10.1016/j.ast.2019.05.038.

[18] A. Magrini, D. Buosi, E. Benini, Analysis of installation aerodynamics and comparison of optimised configuration of an ultra-high bypass ratio turbofan nacelle, Aerosp. Sci. Technol. 128 (2022) 107756, https://doi.org/10.1016/j.ast.2022.107756.

[19] A. Magrini, E. Benini, Aeropropulsive assessment of engine installation at cruise for uhbpr turbofan with body force fan modeling, Aerosp. Sci. Technol. 132 (2023) 108048, https://doi.org/10.1016/j.ast.2022.108048.

[20] A. Magrini, D. Buosi, E. Benini, Maximisation of installed net resulting force through multi-level optimisation of an ultra-high bypass ratio engine nacelle, Aerosp. Sci. Technol. 119 (2021) 107169, https://doi.org/10.1016/j.ast.2021.107169.

[21] I. Goulos, J. Otter, F. Tejero, J. Hueso Rebassa, D. MacManus, C. Sheaf, Civil turbofan propulsion aerodynamics: thrust-drag accounting and impact of engine installation position, Aerosp. Sci. Technol. 111 (2021) 106533, https://doi.org/10.1016/j.ast.2021.106533.

[22] J.J. Otter, I. Goulos, R. Christie, D.G. MacManus, Design and analysis of non-axisymmetric installed aero-engine exhaust systems, Aerosp. Sci. Technol. 106 (2020) 106210, https://doi.org/10.1016/j.ast.2020.106210.

[23] M. Fujino, Y. Kawamura, Wave-drag characteristics of an over-the-wing nacelle business-jet configuration, J. Aircr. 40 (6) (2003) 1177–1184, https://doi.org/10.2514/2.7207.

ARTICLE IN PRESS

JID:AESCTE   AID:108350 /FLA   [m5G; v1.335] P.17 (1-18)

V. Tavares Silva, A. Lundbladh, C. Xisto et al.   Aerospace Science and Technology ••• (••••) ••••••
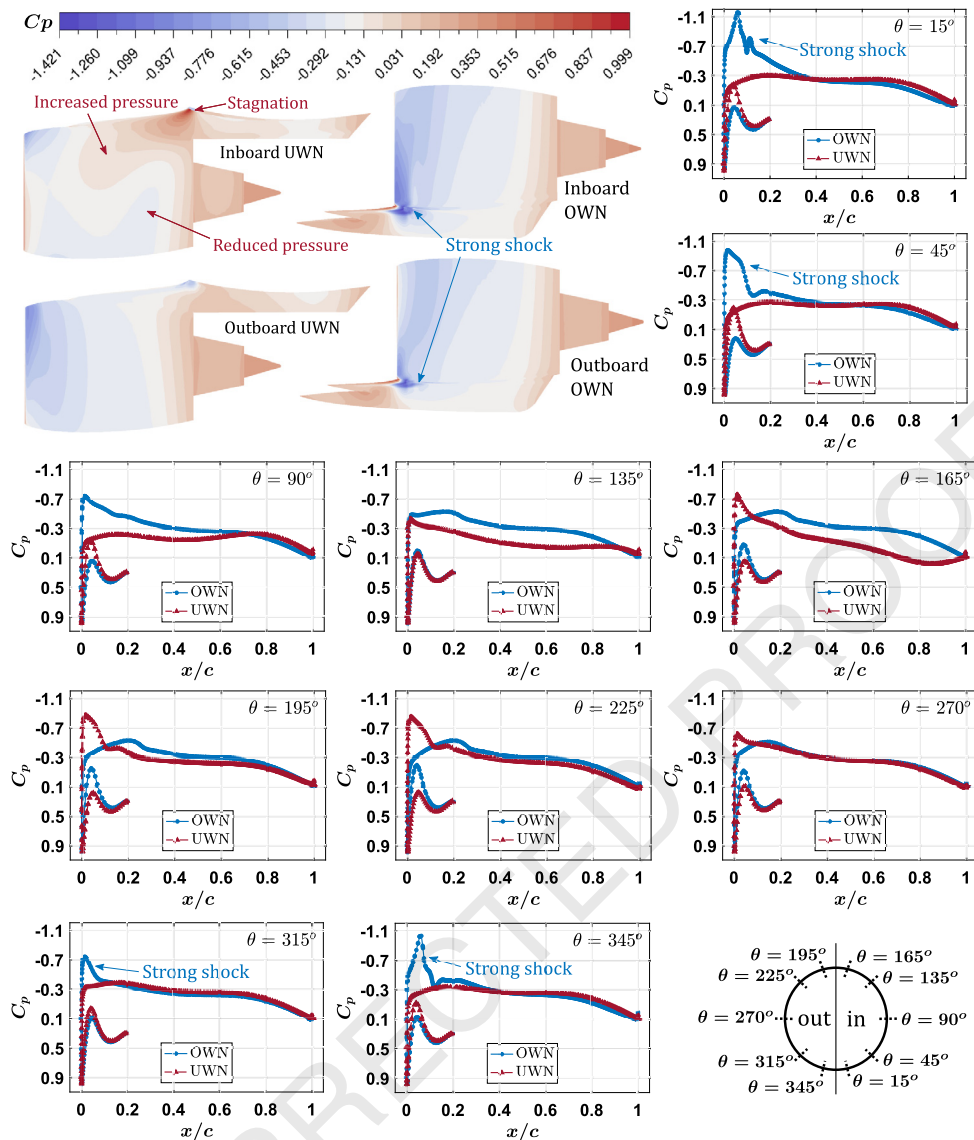
Fig. 24. Contours of pressure coefficient and pressure distributions about the nacelle and inlet for the baseline UWN and the best OWN configurations. $C_l = 0.5$ and $F_{net} = 0$. θ is the circumferential location, starting at the nacelle's keel and increasing counter-clockwise.
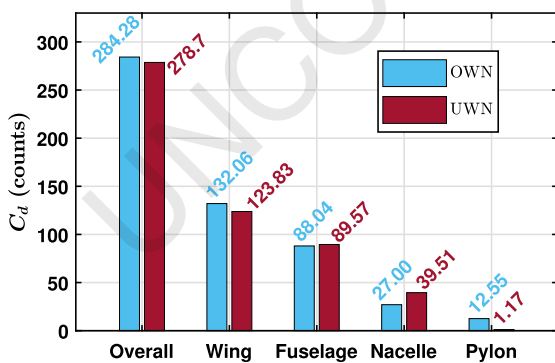

Fig. 25. Drag results for the baseline UWN and the best OWN configurations, including the tail drag. $C_l = 0.5$ and $F_{net} = 0$.

[24] G.A. Hill, O.A. Kandil, A.S. Hahn, Aerodynamic investigations of an advanced over-the-wing nacelle transport aircraft configuration, J. Aircr. 46 (1) (2009) 25–35, https://doi.org/10.2514/1.39730.

[25] S. Berguin, D. Mavris, Interactions in over-wing nacelle optimization, in: 51st AIAA Aerospace Sciences Meeting Including the New Horizons Forum and Aerospace Exposition, 2013, p. 25.

[26] J.R. Hooker, A. Wick, C.H. Zeune, A. Agelastos, Over wing nacelle installations for improved energy efficiency, in: 31st AIAA Applied Aerodynamics Conference, 2013, p. 2920.

[27] J.R. Hooker, Design of a hybrid wing body for fuel efficient air mobility operations at transonic flight conditions, in: 52nd Aerospace Sciences Meeting, 2014, p. 1285.

[28] V.T. Silva, A. Lundbladh, C. Xisto, Aerodynamic installation effects of over-the-wing mounted ultra-high bypass engines, in: 25th International Symposium on Air Breathing Engines, Ottawa, Canada, 2022 (ISABE Paper 2022-145).

[29] M.A.S. Abdul Kaiyoom, A. Yildirim, J.R. Martins, Coupled aeropropulsive design optimization of an over-wing nacelle configuration, in: AIAA SCITECH 2023 Forum, 2023, p. 0327.

[30] F. Lange, R. Rudnik, Numerical position optimization of an over-the-wing mounted engine installation, CEAS Aeronaut. J. 12 (1) (2021) 135–146, https://doi.org/10.1007/s13272-020-00485-4.

[31] P. Wegener, F. Lange, Integration of wing-mounted over-wing engines on a mid-range aircraft, in: AIAA SCITECH 2022 Forum, 2022, p. 2563.

[32] P. Wegener, Integration of Fuselage-Mounted Over-Wing Engines on a Mid-Range Aircraft, ICAS, Shanghai, 2021.

[33] J. Ahuja, S. Ashwin Renganathan, D.N. Mavris, Sensitivity analysis of the over-wing nacelle design space, J. Aircr. 59 (6) (2022) 1478–1492, https://doi.org/10.2514/1.C036687.

[34] B.M. Kulfan, Universal parametric geometry representation method, J. Aircr. 45 (1) (2008) 142–158, https://doi.org/10.2514/1.29958.

[35] F. Zhu, N. Qin, Intuitive class/shape function parameterization for airfoils, AIAA J. 52 (1) (2014) 17–25, https://doi.org/10.2514/1.J052610.

[36] J. Vassberg, M. Dehaan, M. Rivers, R. Wahls, Development of a common research model for applied cfd validation studies, in: 26th AIAA Applied Aerodynamics Conference, 2008, p. 6919.

[37] Pointwise, Pointwise User Manual, Pointwise, Inc., Canonsburg, PA, 2021.

[38] J.C. Vassberg, E.N. Tinoco, M. Mani, B. Rider, T. Zickuhr, D.W. Levy, O.P. Brodersen, B. Eisfeld, S. Crippa, R.A. Wahls, J.H. Morrison, D.J. Mavriplis, M. Murayama, Summary of the fourth aiaa computational fluid dynamics drag prediction workshop, J. Aircr. 51 (4) (2014) 1070–1089, https://doi.org/10.2514/1.C032418.

[39] F.R. Menter, Two-equation eddy-viscosity turbulence models for engineering applications, AIAA J. 32 (8) (1994) 1598–1605, https://doi.org/10.2514/3.12149.

[40] Ansys, Ansys Fluent Theory Guide: Release 2021 r1, ANSYS, Inc., Canonsburg, PA, 2021.

[41] Ministry-Industry Drag Analysis Panel (MIDAP) Study Group, Guide to in-flight thrust measurement of turbojets and fan engines, Tech. rep., Advisory Group for Aerospace Research and Development, 1979, pp. 119–141.

[42] B. Malouin, J.-Y. Trépanier, E. Laurendeau, Installation and interference drag decomposition via rans far-field methods, Aerosp. Sci. Technol. 54 (2016) 132–142, https://doi.org/10.1016/j.ast.2016.04.020.

[43] B. Malouin, M. Gariépy, J.-Y. Trépanier, E. Laurendeau, Engine pre-entry thrust and standard net thrust evaluation based on the far-field method, Aerosp. Sci. Technol. 45 (2015) 50–59, https://doi.org/10.1016/j.ast.2015.04.014.

[44] D. Raymer, Aircraft Design: A Conceptual Approach, American Institute of Aeronautics and Astronautics, Inc., 2012.

[45] E.N. Tinoco, O.P. Brodersen, S. Keye, K.R. Laflin, E. Feltrop, J.C. Vassberg, M. Mani, B. Rider, R.A. Wahls, J.H. Morrison, D. Hue, C.J. Roy, D.J. Mavriplis, M. Murayama, Summary data from the sixth aiaa cfd drag prediction workshop: Crm cases, J. Aircr. 55 (4) (2018) 1352–1379, https://doi.org/10.2514/1.C034409.

[46] D.L. Berry, The Boeing 777 engine/airframe integration aerodynamic design process, in: International Council of the Aeronautical Sciences, in: ICAS Proceedings, vol. 19, 1994, p. 1305 (Paper 94-6.4.4).